Laser shock-induced spalling and fragmentation in vanadium

H. Jarmakani [a], B. Maddox [b], C.T. Wei [a], D. Kalantar [b], M.A. Meyers [a,*]

[a] *University of California, San Diego, La Jolla, CA 92093 0418, USA*
[b] *Lawrence Livermore National Laboratory, Livermore, CA 94550, USA*

Abstract

Polycrystalline and monocrystalline ($\langle 1\,0\,0 \rangle$ and $\langle 1\,1\,0 \rangle$) vanadium was subjected to shock compression followed by tensile wave release to study spall and fragmentation behavior. The shock pulse was generated by a direct laser drive at energy levels ranging from 11 to 440 J mm^{-2} (laser beam irradiated area 1.12 mm^2) and initial pulse durations of 3 and 8 ns (approximate initial pressures between 10 and 250 GPa). Glass and polycarbonate shields placed at a specific distance behind the vanadium targets were used to collect and analyze the ejected fragments in order to evaluate and quantify the extent of damage. The effects of target thickness, laser energy, poly-crystallinity and pulse duration were studied. Calculations show melting at a pressure threshold of $\sim$150 GPa, which corresponds to a laser energy level of $\sim$180 J mm^{-2}. Consistent with the analytical predictions, the recovered specimens and fragments show evidence of melting at the higher energy levels. Spalling in the polycrystals occurred by a ductile tearing mechanism that favored grain boundaries. In the monocrystals it occurred by a mixture of cleavage fracture along the {0 1 0} planes and ductile dimple fracture. This lower spall strength in polycrystals contradicts predictions from the Hall–Petch equation. Experimentally obtained fragment sizes were compared with predictions from the Grady–Kipp model. The spall strength of vanadium under laser loading conditions was calculated from both VISAR pull-back signals and using the spall thickness. It was found to be considerably higher than predictions from gas gun experiments, the monocrystals showing a higher value than polycrystals. This higher spall strength is suggestive of a strong time dependence of the phenomenon, consistent with the nucleation and growth kinetics of voids and the strain rate sensitivity embedded in the Grady theory.

© 2010 Acta Materialia Inc. Published by Elsevier Ltd. All rights reserved.

Keywords: Impact behavior; Fracture; Laser treatment; Vanadium; Schock

1. Introduction

The dynamic spalling and fragmentation of metals induced by laser irradiation is a concern of great significance to the successful operation of the National Ignition Facility (NIF). Protection from spalling and fragmentation is necessary to preserve the functionality of the laser optics systems and diagnostic tools of the main target chamber. In particular, vanadium is a candidate material for first wall and blanket components of fusion power systems because of its low irradiation-induced activity, high stability and good compatibility with lithium [1–3].

Studies on the extent of damage to metal targets and their surroundings caused by laser impingement on the surface are scarce. Spall is the dynamic fracture that takes place inside a solid body as a result of tensile stresses that develop due to the interaction of propagating waves. Compressive waves traveling from the energy deposition surface of a body intersect those reflecting from the rear surface, causing internal ruptures, or spallation, if the tensile stresses are sufficiently high. Damage accumulation takes place in four stages: (a) nucleation of voids or cracks at existing damage sites; (b) growth of individual voids or cracks; (c) coalescence of voids or cracks; (d) fragmentation [4–6]. Much of the research on dynamic fracture has been carried out under planar flyer plate impact [7–11] and high explosive detonation [12–16]. These typical methods of

* Corresponding author. Tel.: +1 858 534 4719; fax: +1 858 534 5698.
E-mail address: mameyers@ucsd.edu (M.A. Meyers).

generating shock waves produce pressures less than 100 GPa and pulse durations of a minimum of 50 ns.

Only recently have laser-driven shock experiments begun to gain momentum [16–28]. The advantages of using high intensity lasers to produce shocks in metals lie in the fact that extremely high pressures (in the TPa range) and strain rates ($\sim 10^9 \, \text{s}^{-1}$) can be achieved with pulse durations of only a few nanoseconds. More accurate microstructural characterization is also possible due to the self-quenching mechanism associated with laser shock (discussed in detail by Meyers et al. [29] and Cao et al. [30]). Interestingly, almost no research has been carried out on the dynamic behavior of materials shocked above their melting pressures. A notable exception is a study by Rességuier et al. [31] on liquid spall in laser-shocked tin. Lubarda et al. [32] looked at void growth in copper induced by a laser. Little is known about the process of material ejection from the spalled surface of laser-shocked samples and the fragmentation, spreading of debris and extent of damage to surrounding objects.

Earlier findings of considerable interest were the lower spall strength exhibited by polycrystalline than monocrystalline copper. This contradicts the Hall–Petch equation and has been attributed to the existence of nucleation sites at grain boundaries in the polycrystals by Christy et al. [33] and Kanel et al. [34]. Meyers [35] also discussed this and provided an interpretation based on the greater availability of nucleation sites in the polycrystals. Another issue of importance is the pulse length dependence of spall strength. In support of spalling as a nucleation, growth and coalescence process, Gray and co-workers [36,37] demonstrated that for stainless steel and copper it is time-dependent, being higher for the triangular pulse than for a square pulse generated by flyer plate impact. Gilath [38] reported a two to threefold increase in the spall strength of aluminum in laser experiments in comparison with gas gun spalling reported by Grady [39].

This previous research was the motivation for the investigation whose results are reported herein: the spalling and fragmentation of vanadium induced by laser irradiation.

2. Experimental procedure

The polycrystalline vanadium foils used in this work were obtained from Alpha Aesar and had a purity of ~99.8%. Three different foil thicknesses were used: 75, 127 and 250 μm. Polycrystalline specimens from each of the three as received foils were cut, polished and etched to measure the grain size. Monocrystalline specimens with the orientations ⟨1 1 0⟩ and ⟨1 0 0⟩ and thickness 250 μm were used. They were obtained from Accumet Materials and had a reported purity of ⩾99.999%.

The specimens were polished using 1200, 2400 and 4000 grit paper, followed by 0.3 and 0.05 μm alumina compound. The etchant used was a mixture of 1 ml HF, 30 ml HNO_3 and 30 ml lactic acid. Micrographs of the grains revealed after etching are shown in Fig. 1, and a

summary of the grain sizes and aspect ratios are given in Table 1. All specimens exhibited grain elongation due to rolling.

The laser experiments were conducted at the Jupiter Laser Facility, Lawrence Livermore National Laboratory. Fig. 2 is an illustration of the cross-sectional view of the experimental set-up. Fig. 2a shows the general set-up of the experiment and Fig. 2b and c are depictions qualitatively showing the damage that occurred to the vanadium targets as the thickness changes. Fig. 2b shows complete blow-off of the thinnest vanadium samples; Fig. 2c shows blow-off surrounded by a spall surface in the intermediate thickness samples; Fig. 2d shows only spall that occurs in the thickest samples.

A Nd glass laser with a 532 nm pulse width was used to generate high pressure laser-driven shocks in the vanadium samples. Both 3 and 8 ns square pulse lengths were used to study the effect of pulse duration on material behavior. A 1 mm kineform phase plate (KPP) was used to generate a flat intensity profile that was ~1 mm square in size. The vanadium samples were cut into small 3.5 × 5 mm rectangles and glued between two steel washers having a 10 mm outer diameter and 2.5 mm inner diameter. Glass slides were placed parallel to the targets, approximately 12 cm behind, to collect vanadium fragments and to analyze the resultant damage. The associated laser energies and pulse durations of the polycrystalline samples investigated are tabulated in Table 2. The pressure at the rear surface of the vanadium targets was determined by measuring the free surface velocity using the VISAR technique [40]. The velocity interferometer was configured in the Mach–Zender geometry and coupled to a Hamamatsu streak camera set to a 50 ns sweep to provide a time-dependent pressure history [41]. The spatial scale of the line in VISAR was around 800 μm at the target plane. The central ~100 μm of that region was used.

The Doppler shift of light reflected off the back surface of the targets was observed as a phase shift in the fringe pattern recorded by the streak camera. The fringe phase φ is related to the velocity of the reflecting surface u by:

$$\frac{\lambda \varphi}{4 \pi \tau (1 + \delta)} = u \tag{1}$$

where λ is the wavelength of the VISAR probe laser and τ is the optical delay produced by a glass etalon in the interferometer. This optical delay can be calculated for a given etalon of thickness d and index of refraction n by:

$$\tau = \frac{2d(n - 1/n)}{c} \tag{2}$$

where c is the velocity of sound. Dispersion in the etalon introduces a wavelength-dependent correction δ [42]. For the 532 nm wavelength probe laser used in this study $\delta = 0.0318$.

When a shock wave reaches the VISAR probe surface the resulting fringe phase jump is discontinuous and the number of 2π phase jumps cannot be uniquely determined
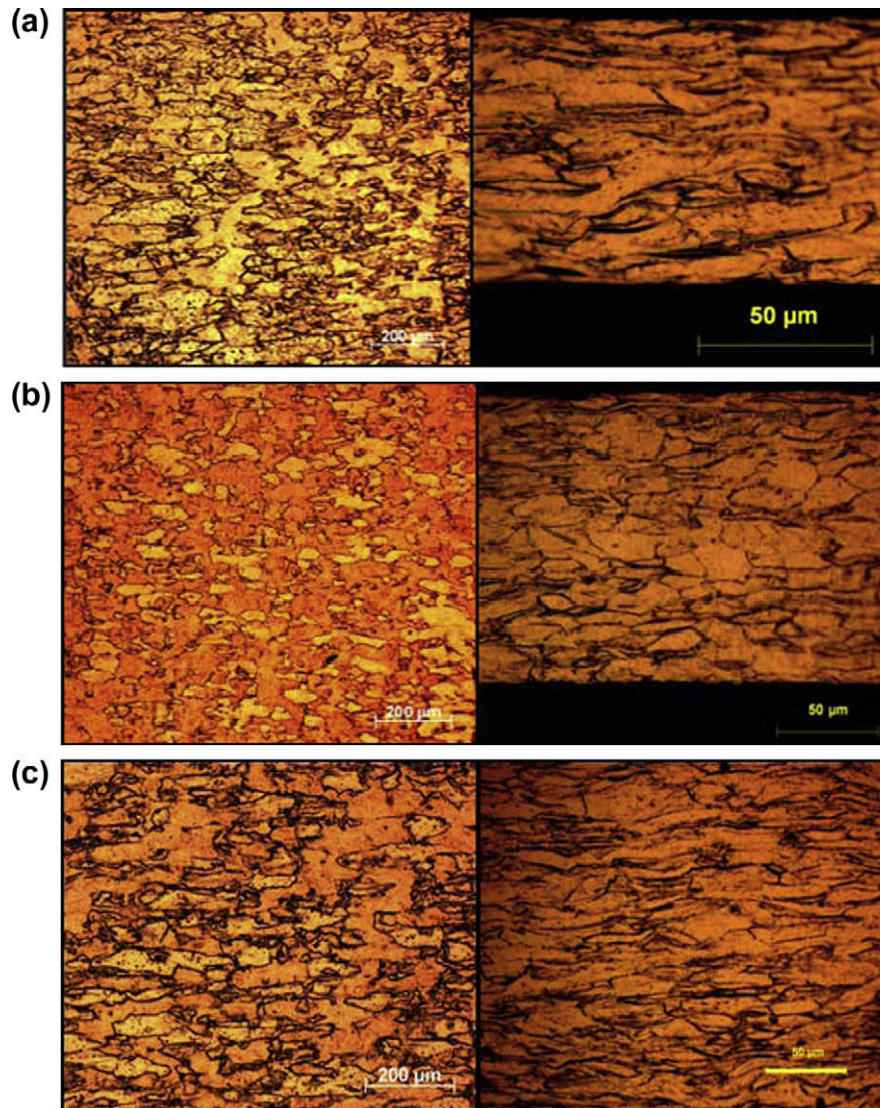
Fig. 1. Grains revealed after etching of top/bottom surface (left) and cross-section (right) of samples: (a) 75 μm thickness; (b) 127 μm thickness; (c) 250 μm thickness.

Table 1
Grain sizes of as received vanadium foils.

Thickness (μm)	Top/bottom surface		Cross-section surface	
	Grain size (μm)	Aspect ratio	Grain size (μm)	Aspect ratio
75	100	3.5:1	16	6:1
127	64	2.4:1	20	3:1
250	126	4:1	13	8:1

using a single VISAR interferometer alone. Thus, two independent interferometers using two different etalon thicknesses, $d_1 = 50.074$ and $d_2 = 28.77221$ mm, were employed to resolve this fringe jump ambiguity. By setting $\varphi = 2\pi$ in Eq. (1), one can calculate the velocity sensitivity in km s^{-1} fringe^{-1} for a given optical delay or etalon thickness. For the etalons used in this study, the velocity sensitivities were calculated to be 0.995041093 and 1.731729599 km s^{-1} fringe^{-1} for d_1 and d_2, respectively.

3. Results and discussion

Section 3.1 presents the calculated pulse decay using both a simplified and the HYADES methods. Section 3.2 presents a thermodynamic analysis determining the melting temperature as a function of pressure, which enables calculation of the critical pressure for melting. Section 3.3 provides a detailed characterization of the recovered specimens in order of increasing thickness. Section 3.4 presents results of monocrystalline experiments. Section 3.5 shows the shadowgraphs of the in-flight fragments. Section 3.6 involves fragment size modeling of vanadium due to spalling. Section 3.7 discusses spall strength calculations of vanadium based on the laser shock experiments.

3.1. Calculated pulses using HYADES and tantalum results

The calculated pressures and decay profiles using the one-dimensional HYADES code are shown in Fig. 3a. The
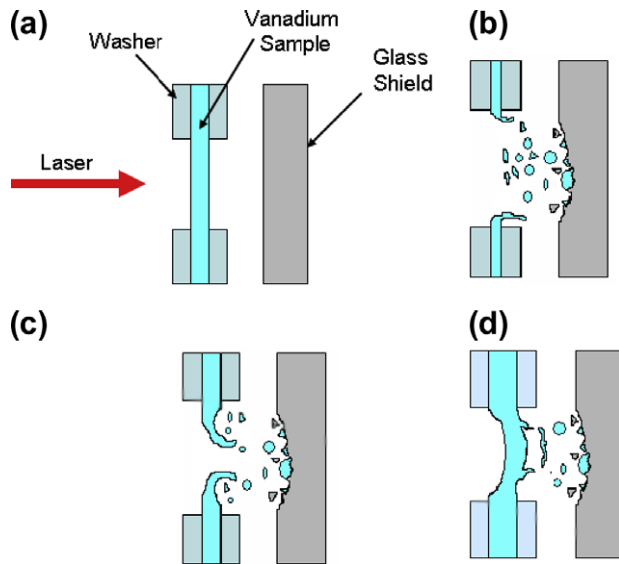
Fig. 2. (a) Schematic of the cross-sectional view of the experimental set-up; (b) laser shock of thinnest target; (c) laser shock of intermediate thickness target; (d) laser shock of thickest target.

Table 2
Laser energy and pulse duration of experiments.

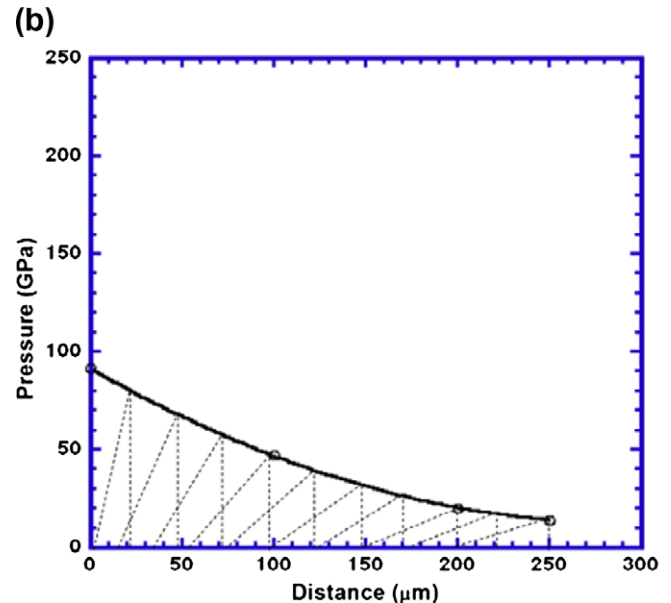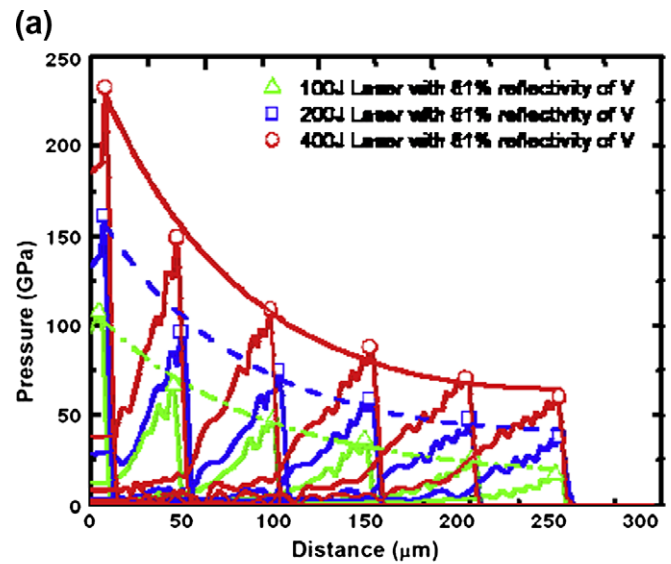| Experiment	Foil thickness (μm)	Energy (J)	Diagnostic	Pulse length (ns)
3	75	290	Glass shield	3
4	75	167	Glass shield	3
5	127	228	Glass shield	3
8	250	438	Glass shield	3
9	127	430	Glass shield	3
11	250	251	Glass shield	3
12	250	442	Aerogel	3
13	127	381	Aerogel	3
14	127	209	Aerogel	3
15	75	199	Aerogel	3
18	127	218	Glass shield	8
22	127	218	Glass shield	8

Fig. 3. (a) HYADES code simulation of laser pulse propagation in vanadium with 61% reflectivity [*] from simulation by. ○ represents 400 J laser propagated in V: initial pressure 234 GPa; free surface pressure 60.1 GPa; duration of propagation ~32 ns. □ represents 200 J laser propagated in V: initial pressure 161 GPa; free surface pressure 37.5 GPa; duration of propagation 36 ns. Δ represents 100 J laser propagated in V: initial pressure 107 GPa, free surface pressure 16.4 GPa; duration of propagation 41.1 ns. (b) Calculated decay of pulse propagation for initial energy of 100 J.

pressure pulse decay profiles were calculated at the three different energy levels around which the experiments were conducted: 100, 200 and 400 J. The results were calibrated for the reflectivity of vanadium, taken as 61% [43]. The pressures decayed rather rapidly as the pulse duration increased. The triangular nature of the pulse shape was retained throughout propagation in the 250 μm thick specimens. The initial pressures, which were equal to 107, 161 and 234 GPa for the three energy levels (100, 200 and 400 J), were reduced to approximately one-quarter of their original values at the free surface.

The pressure profiles were also computed based on calibrated laser shock experiments on tantalum carried out at 200 J (D. Eder, unpublished work). The conversion of parameters from tantalum to vanadium was carried out using the conservation of energy equation:

$$\Delta E = \frac{1}{2} U_p^2 \tag{3}$$

where ΔE is the change in energy and U_p is the particle velocity. The internal energy inside the shock-compressed mate-

rial is a function of the laser energy and, to a first approximation, we assumed that this function is material independent. Differences in reflectivity between vanadium (61%) and tantalum (78%) were neglected. The experimental pressure values as a function of distance into the material obtained from the tantalum experiments (D. Eder, unpublished work) are listed in Table 3. The predicted pressure pulse decay profiles in vanadium for an input energy of 100 J is presented in Fig. 3b. It can be seen that the results in Fig. 3a and b are fairly consistent. Experimental predictions using the tantalum results match the HYADES calculations fairly
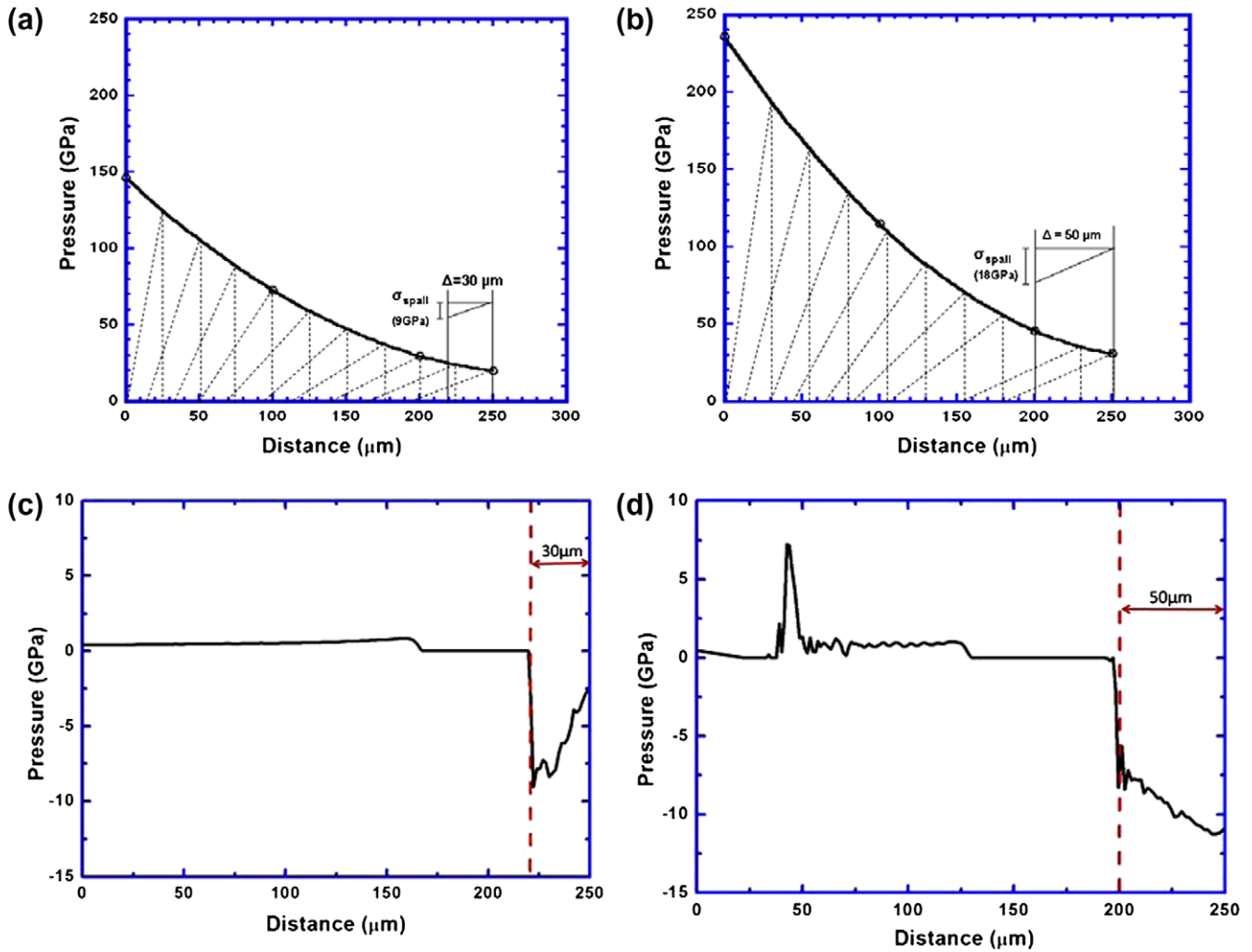
Fig. 4. Spall strength estimation from spall plane: (a) predicted pulse decay from calculation at 200 J; (b) from calculation at 400 J; (c) HYADES computation at 200 J; (d) HYADES computation at 400 J.

well. Fig. 4a and b show the pressure decay for energies of 200 and 400 J calculated from Eq. (3). The rate of decay of the pulse was a little lower for HYADES, leading to higher pressures at the spall side of the specimens.

The spall strength was calculated by two methods: using the thickness of the spall regions and by VISAR velocimetry, through the pull-back signal technique. The thickness of the spall layer can be used to obtain a simple estimate of the spall strength through the schematic representation of Fig. 5. The spall strength σ_T is shown in the reflected portion of the wave. The distance Δ represents the distance that the reflected wave had traveled until it reached the level at which the material spalled. The relationship between P, the maximum stress at the back surface, Δ and σ_T is, for a perfectly triangular pulse having a length L [38]:

$$\sigma_T = \frac{2\Delta}{L} P \qquad (4)$$

Eq. (4) was used to obtain the spall strengths of specimens in which Δ could be established in a clear and incontrovertible manner. The results are discussed in Section 3.7

3.2. Modeling of melting of vanadium under shock compression

The temperature rise due to shock and the melting temperature as a function of pressure were computed in order to determine the theoretical pressure at which vanadium will melt when subjected to a shock. The Clausius–Clapeyron relation describes the effect of pressure on the temperature at which a phase transition occurs between two states of matter (see, for example, [44]). For melting, this relation is given by:

$$\frac{dP}{dT} = \frac{\Delta H_m}{T \Delta V_m} \qquad (5)$$

where H_m is the enthalpy of fusion at the melting point (422 J g^{-1}) and V_m is the volume change associated with melting, assumed to be independent of pressure. V_m for vanadium is expressed as:

$$\Delta V_m = \frac{1}{\rho_{T_m}} - \frac{1}{\rho_{T_o}} \left(1 + \frac{\Delta V}{V_o} \right) \qquad (6)$$

Table 3
Pressure and U_p values as a function of distance obtained from laser shock experiments on tantalum from D. Eder (unpublished report).

Distance (µm)	Pressure (GPa)	U_p (km s^{-1})
100	150	1.664
200	60	0.819
250	40	0.584

where V/V_o is the change in volume from T_o to T_m, ρ_{T_m} is the density of solid vanadium at the melting temperature (5.76 g cm^{-3}, determined from Sorkin et al. [45], which indicated that $[V(T_m)]/[V(T_o)] = 1.06$), ρ_{T_o} is the density at ambient temperature and pressure (6.11 g cm^{-3}) and V/V_o is given by:

$$\Delta V/V_o = 3\gamma T_m \tag{7}$$

where γ is the thermal expansion coefficient, 8.4×10^{-6} K^{-1}, and T_m is the melting temperature of vanadium, 2183 K. Rearranging Eq. (5), integrating and solving for melting temperature as a function of pressure yields the following expression that relates the melting temperature to pressure:

$$\int_{(T_m)_o}^{(T_m)_P} \frac{dT}{T} = \frac{\Delta V}{\Delta H} \int_{P=0}^{P} dP$$
$$\rightarrow \ln(T_m)_p = \frac{\Delta V}{\Delta H} P + \ln(T_m)_o \tag{8}$$

The temperature rise induced by shock compression has been extensively analyzed and modeled in the literature (see, for example, [44]). The shock temperature rise can be calculated using the following equation:

$$T_s = T_o \exp\left[\frac{\gamma_o}{V_o}(V_o - V_1)\right] + \frac{P(V_o - V_1)}{2C_v}$$
$$+ \frac{\exp\left[\frac{-\gamma_o}{V_o} V_1\right]}{2C_v} \int_{V_o}^{V_1} P \exp\left(\frac{\gamma_o}{V_o} V\right)\left[2 - \frac{\gamma_o}{V_o}(V_o - V)\right] dV \tag{9}$$

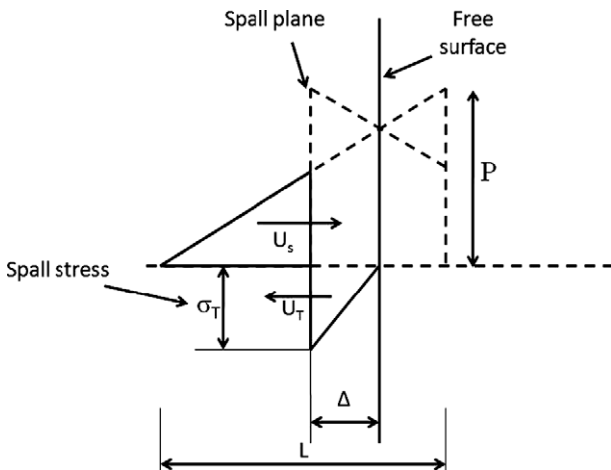where γ_o is the Grüneisen parameter (two for vanadium [45]), C_v is the specific heat capacity (489 J kg K^{-1}) and V_o and V_1 are the initial and current specific volumes of the material, respectively. The pressure dependence on volume or the Hugoniot is given as:

$$P = \frac{C_o(V_o - V)}{[V_o - S(V_o - V)]^2} \tag{10}$$

V_1 can be calculated from the relationship [44]:

$$V_1 = \frac{C_o^2}{2PS^2}\left[\sqrt{1 + \frac{4PSV_o}{C_o^2} + \frac{2S(S-1)V_oP}{C_o^2}} - 1\right] \tag{11}$$

The melting temperature (determined from the Clausius–Clapeyron relation) and the shock temperature rise as a function of pressure are given in Fig. 6. The melt curve determined by the Clausius–Clapeyron relation (red solid line) is in agreement with experimental work carried out by Jephcoat et al. [46]. Their work was, however, confined to pressures up to 100 GPa. Interestingly, our modeling captured the surprisingly small melting slopes seen in bcc metals, which were clearly documented in extensive work by Errandonea et al. [47]. The predicted shock temperature profile (solid black line) is in agreement with data reported by McQueen et al. [48] up to a pressure of ~160 GPa, where it begins to deviate. The plot shows that vanadium remained solid up to a pressure of ~150 GPa, after which it melted. Our predicted melting pressure of 150 GPa is lower than results obtained experimentally by Dai et al. [49], who determined a melting pressure of ~250 GPa. We also plotted the release curve for vanadium from McQueen et al. [48]. The release curve lies below the melt curve, suggesting that any material that melts under shock will be quenched back to the solid state upon release.
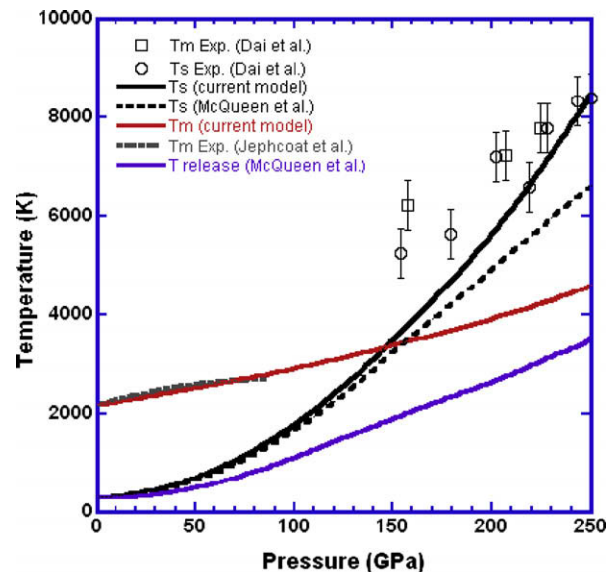

Fig. 5. Calculation of spall strength from reflected pulse at free surface.

Fig. 6. Shock temperature rise and melting temperature as a function of pressure.

3.3. Characterization of samples

Analysis and characterization of the samples were carried out by optical and scanning electron microscopy (SEM), and the findings are presented in four sections in the order of increasing thickness of the samples: polycrystals 75 (Section 3.3.1), 127 (Section 3.3.2) and 250 μm (Section 3.3.3) thick and 250 μm thick monocrystals (Section 3.4).

3.3.1. Experiments on 75 μm thick targets

Three 75 μm thick samples were laser-shocked at energy levels of 167, 199 and 290 J and at an initial pulse duration of 3 ns. Almost complete blow-off occurred in all the samples, as shown in Fig. 7a, except for small portions around the hole in the washer that remained. Fig. 7b shows an SEM image of the surface of the "lip" that remained after

irradiation in the 167 J experiment. The exposed grains from the spall region show the characteristic elongated configuration. The blow-off surfaces of the samples where vanadium was ejected revealed a flaking phenomenon mostly attributed to grain boundary separation. Separation along grain boundaries can also be clearly seen in Fig. 7c, for 199 J, which also captures grain elongation along the rolling direction.

The samples shocked at 167 and 290 J had glass shields placed behind them, whereas the sample shocked at 199 J had an aerogel set-up (aerogel experiments are not discussed in this study). Because of their thinness, a significant amount of vanadium was ejected onto the glass shields as compared with samples having a greater thickness. Most of the damage and rubble was collected at the center of the glass shields. Fig. 8 shows micrographs of the damage on the surface of the glass shields induced by vanadium
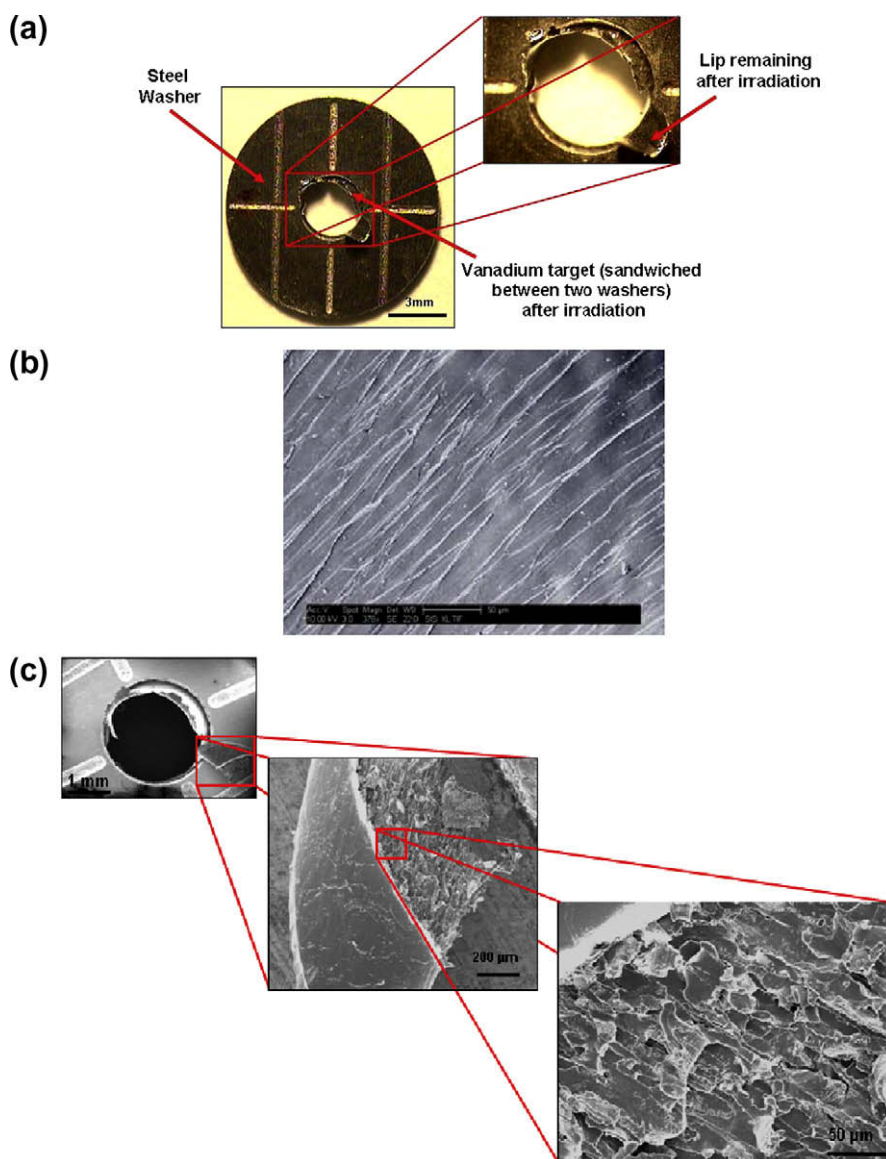

Fig. 7. (a) 75 μm thick polycrystalline specimen after laser shock, 167 J; (b) surface of "lip" showing elongated grains, 167 J; (c) blow-off surface of 75 μm thick samples showing flaking due separation along grains, 199 J.
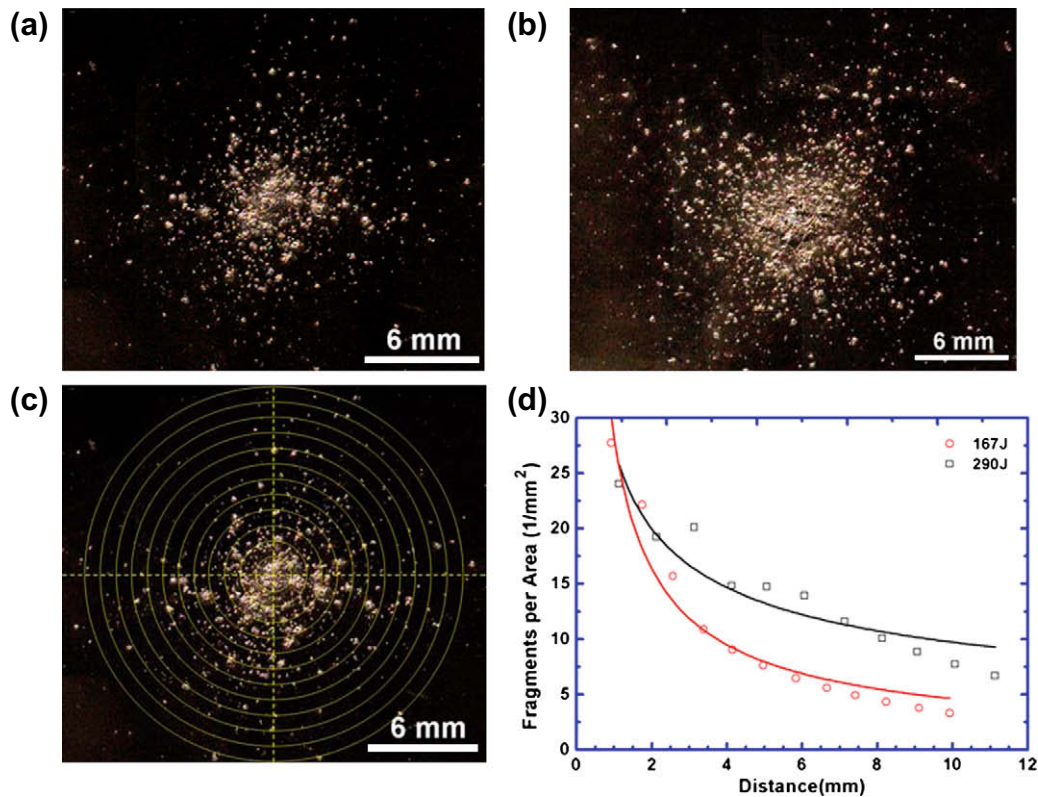
Fig. 8. Glass shields damaged by polycrystalline vanadium, 75 μm; (a) 167 J; (b) 290 J; (c) circular grid placed on glass shield for fragment quantification; (d) fragments per area as a function of distance from central damage.

fragments for both the 167 and 290 J experiments (Fig. 8a and b). Clearly, the extent of damage from the ejected fragments was greater in the 290 J experiment. In order to quantify the damage to the glass shields induced by the vanadium fragments, a circular grid was superimposed on the glass shield images, as shown in Fig. 8c, and the imaging software ImageJ was used to help determine the number of fragments per unit area as a function of distance away from the central damage zone. Clearly, the plot in Fig. 8d shows that the extent of damage (fragments per unit area) to the 290 J glass shield was more significant compared with the 167 J glass shield. The experimental data are well matched by a power function. Note the reduction in damage away from the central crater.

SEM images of the glass shields revealed that vanadium debris collected in two forms: solid fragments and molten/resolidified fragments. In the case of the 167 J experiment solid vanadium fragments and "splashes" were evident around the edges of the central crater (Fig. 9). Fig. 9a shows the main central crater and the damage induced by the vanadium. Fig. 9b is a close-up view of an area around the crater showing mostly vanadium flakes and occasional "splashes" (circled). It should be noted that the occurrence of resolidified vanadium around the crater was less frequent than in the 290 J experiment. Fig. 9c shows a high density of vanadium debris around the central crater. This image is a close-up of the area within the box highlighted in Fig. 9a.

SEM analysis of the glass shield from the 290 J experiment showed more significant damage and greater melting of vanadium around the edges of the central crater (Fig. 10a). Note the radial and circumferential cracks on the glass surface due to the vanadium fragments. Fig. 10b shows larger vanadium fragments surrounded by vanadium "splashes". Fig. 10c is a higher magnification SEM image of the resolidified vanadium. The image to the right suggests that the vanadium particle was ejected in liquid form from the target and formed a solid outer shell enclosing an inner liquid core as it traveled towards the glass shield. Upon impact the outer shell was squashed releasing the inner liquid core around it.

It should be noted here that the melting and shock temperature rise modeling (Fig. 6) suggests that any vanadium that melts under shock compression should resolidify upon release, since the release curve (blue line)[1] lies beneath the melt curve (red line). As observed from the SEM results, melting of vanadium did indeed occur in the experiments. This implies that melting must have occurred under shock and not release (known as high pressure melting). A survey of the literature suggests that this phenomenon is uncommon. Furthermore, the very short pulse durations (3 ns) in the experiments provided very little time for the material

---

[1] For interpretation of color in Figs. 1–4, 6–13, 16–20 and 23–28, the reader is referred to the web version of this article.
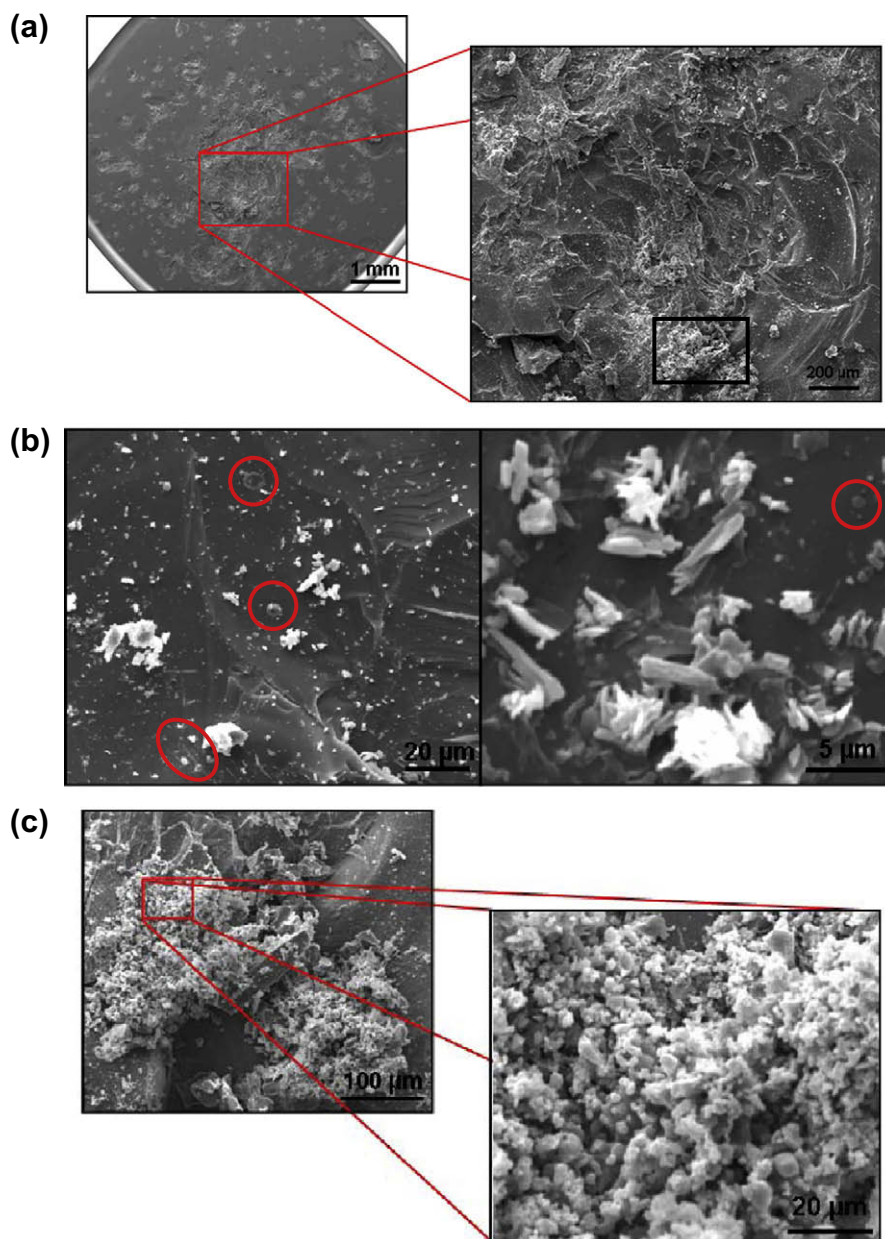
Fig. 9. Glass shield of 75 μm polycrystalline specimen shocked at 167 J, 3 ns; (a) central crater; (b) vanadium particles near center crater; (c) vanadium debris near central crater.

to solidify upon release, which is probably why we observed melting on the glass shield. Melting upon impact with the glass shield is also a likely scenario.

Energy dispersive X-ray spectroscopy (EDS) was conducted on the glass shields and the energy spectrum was analyzed to confirm the elements present. Elemental analysis of the large fragment corresponding to the dotted square and the background/glass shield within the area of the small solid square was conducted and confirmed that it was indeed vanadium.

3.3.2. Experiments on 127 μm thick targets

The 127 μm vanadium targets that were analyzed in this study were subjected to the following laser energies: 209,

218, 228, 381 and 430 J. The 209 and 381 J experiments had aerogels placed behind the targets instead of glass shields (only the targets are studied in these cases) and two 218 J experiments were carried out with both glass shield and aerogel set-ups. The pulse duration in all cases was 3 ns, except for the 218 J experiment, where it was 8 ns. The 218 and 228 J experiments provided a means to compare the effect of the change in pulse duration at comparable laser energies. In all cases, the target showed tearing away around the square laser spot and a spall surface formed around the hole or area blown off, as shown in Fig. 11 for one of the 218 J experiments. The vanadium sample pertaining to the 218 J, 8 ns experiments had a slightly larger blow-off diameter compared with the 209 J,
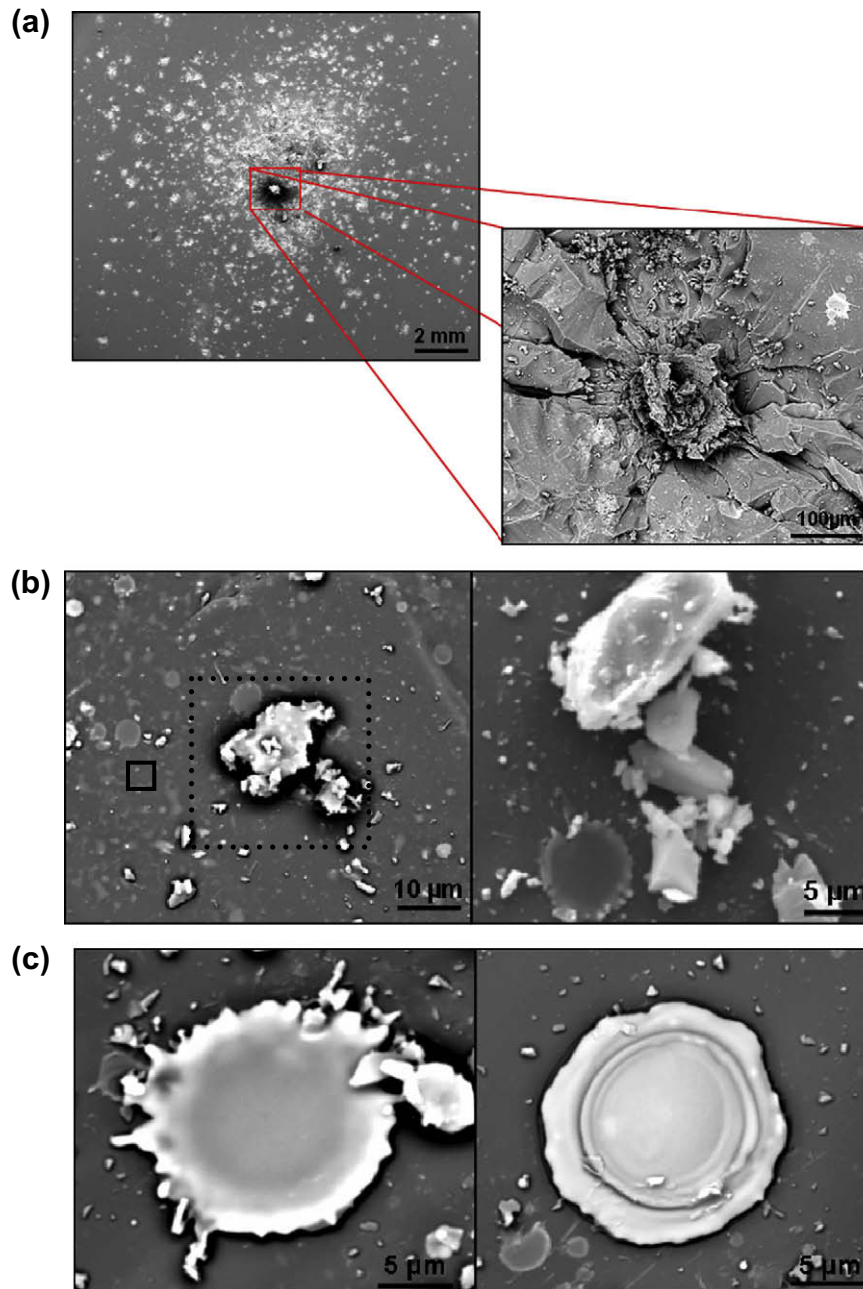
Fig. 10. (a) Glass shield of 75 μm specimen shocked at 290 J, 3 ns: (a) central crater with radial and circumferential cracks; (b) Solid particles and fragments; (c) particles that were molten upon impact, 290 J.

3 ns experiment, probably due to both the increased pulse duration and slightly higher energy level.

More material around the laser spot survived compared with the 75 μm thick targets (Fig. 11a). Direct interaction of the laser beam with the vanadium surface also caused melting. Flaking and peeling away along the grain boundaries can clearly be seen in Fig. 11b and dimpling and void formation on the blown-off surface was also evident (Fig. 11c), which are characteristics of ductile behavior. These features typically form as a result of void nucleation, growth and coalescence. The blow-off diameter increased with pulse duration. Fig. 12 shows the increase in blow-off diameter as the laser energy was increased.

The glass shields analyzed showed a clear effect of the increase in laser energy and pulse duration. Much more damage and debris accumulated on the glass shields at the higher energy levels. Fig. 13 shows images of the cratered surfaces of the glass shields placed behind the 127 μm thick targets. The glass shield in Fig. 13a was placed behind the target subjected to a 218 J pulse having a duration of 8 ns, whereas the glass shield in Fig. 13b represents the 3 ns pulse at 228 J. The higher pulse duration does not seem to have increased the amount of damage to the glass shield. However, it resulted in larger fragments being ejected from the vanadium targets, as would be expected. In fact, the damage on the glass
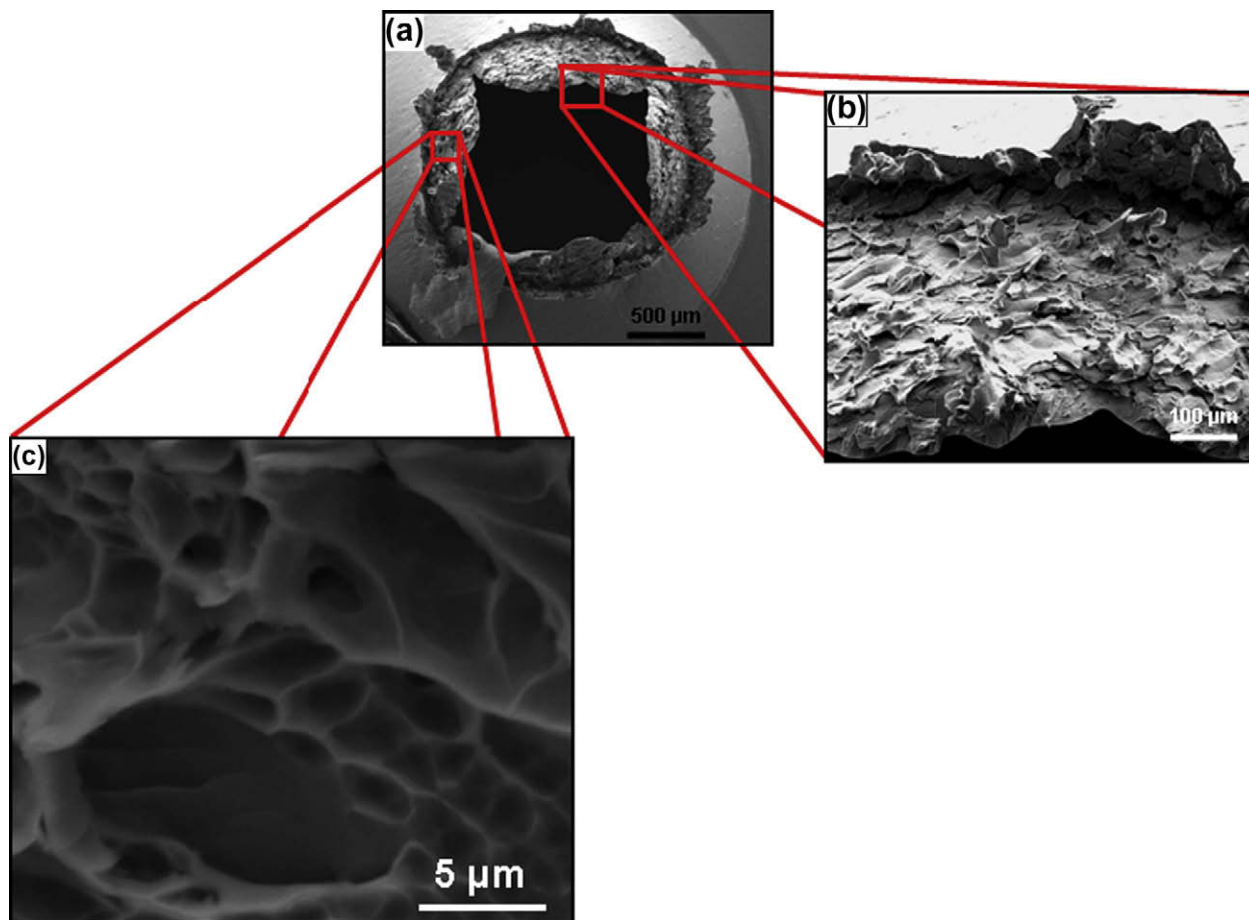
Fig. 11. 127 μm thick specimen after laser shock, 218 J, 8 ns; (a) overall view showing blow-off and spalled region; (b) flaking due to grain boundary separation; (c) dimples and voids.

shield subjected to the 3 ns pulse was significantly greater. Fig. 13c shows the surface of the glass shield behind the target subjected to 430 J. Clearly, a greater amount of vanadium was ejected onto the glass shield, causing more damage. One can see the geometrically square nature of the central damaged zone in Fig. 13c, which is due to the square geometry of the laser focal spot incident on the target. Fig. 13d is a plot showing quantification of the fragments on the glass shields. Clearly, the fragments per unit area increased as the laser energy increased. The experimental results were fitted to power functions that describe well the rapid rise in fragment density close to the center of the target.

SEM images of the glass shields revealed that a more significant amount of vanadium melted and splashed onto the surface in the case of the 8 ns laser pulse at the lower energy level. Fig. 14 shows the greater degree of melting that occurred in the 218 J, 8 ns experiment as compared with the 228 J, 3 ns experiment. The glass shield placed behind the target subjected to a 3 ns pulse at 430 J revealed the greatest amount of melting (Fig. 15). At this highest energy level tiny vanadium fragments in the form of whiskers (~3 μm in length) were evident and spread around the main cratered region.

3.3.3. Experiments on 250 μm thick targets

The 250 μm thick vanadium targets were subjected to a laser beam at the following energies: 251, 438 and 442 J.
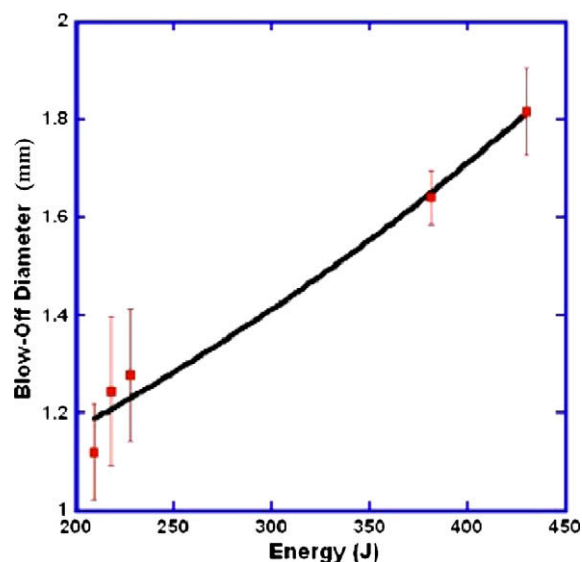

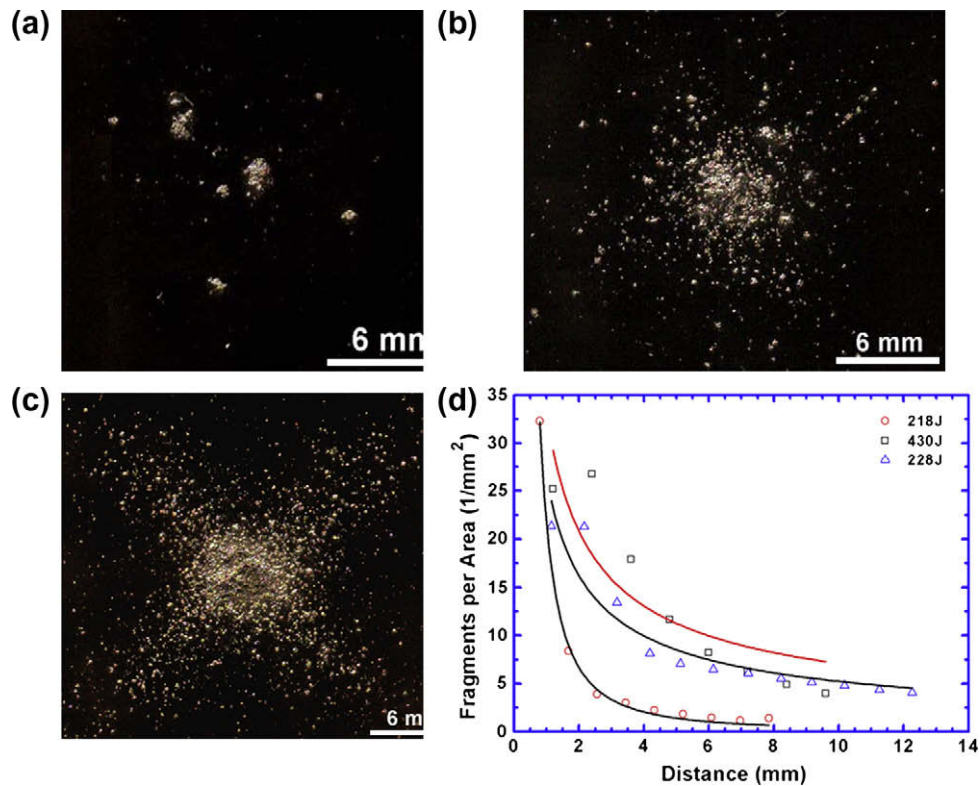Fig. 12. Blow-off diameter of 127 μm thick specimens.

Fig. 13. Glass shields placed behind 127 μm thick targets; (a) 218 J, 8 ns; (b) 228 J, 3 ns; (c) 430 J, 3 ns; (d) fragments per area vs. distance from central crater.
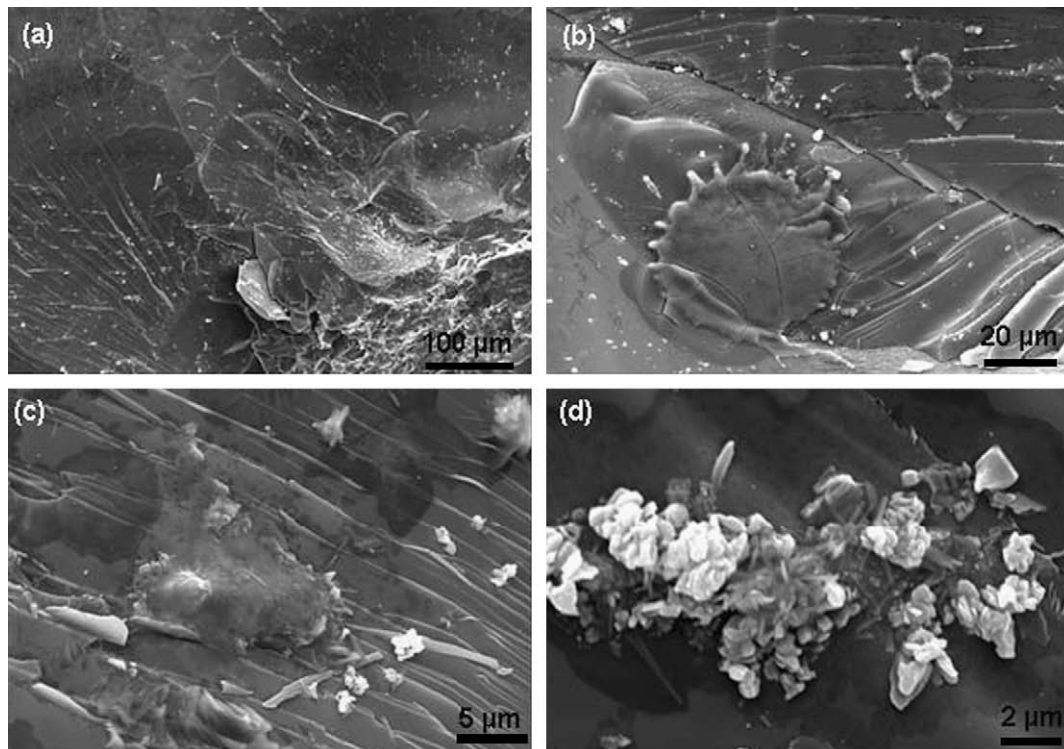

Fig. 14. (a) SEM images of glass shield behind 127 μm thick target, 218 J, 8 ns; (a) damage around edges of crater; (b) splashes around central crater; (c) molten and solid vanadium particles; (d) vanadium clumps.
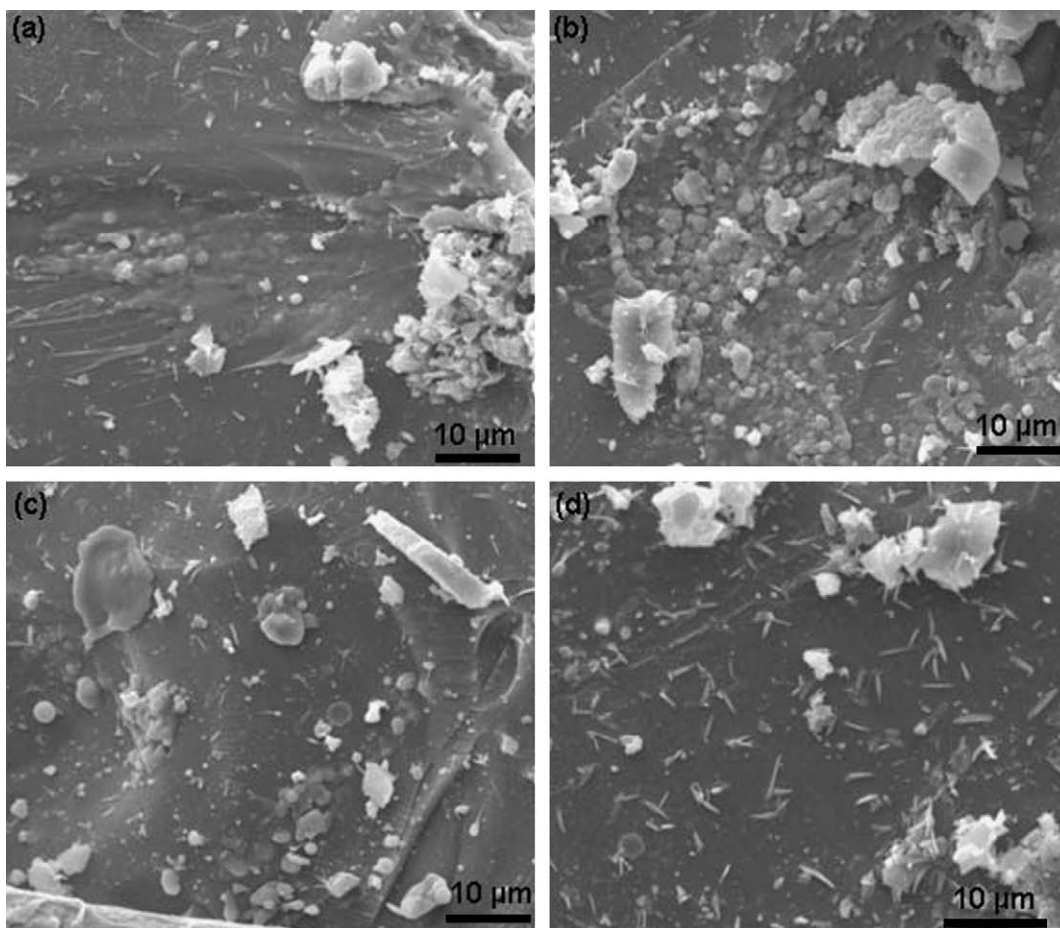
Fig. 15. SEM images of glass shield behind 127 μm thick target, 430 J, 3 ns: (a) vanadium splashing around edges of central crater (b and c) vanadium debris, both solid and splashes; (d) vanadium whiskers.

The pulse duration in all cases was 3 ns (the 442 J experiment had an aerogel diagnostic). Because of the increased thickness, the targets were not punctured through. Instead, a spall plane formed on the back surface of all the 250 μm targets where vanadium was ejected from the surface (Fig. 16). Even the sample subjected to 50 J energy showed complete separation. The fibrous appearance of the fracture is consistent with separation along grain boundaries, which is discussed below. Fig. 17 is a plot of the spall diameter as a function of laser energy for both the 250 μm and 127 μm targets (the spalled area around the tear-off region is considered in the case of the 127 μm targets). The plot shows an increase in spall diameter (and, hence, spall surface area) as the energy increased. The spall diameter in the 127 μm targets was, however, larger than that in the 250 μm targets. The 251 J sample was sectioned and mounted in order to better analyze the spall surface. Fig. 18 shows cross-sections of the specimen. Flaking, separation along the grains, cracking and the formation of voids close to the surface are evident.

Again, the glass shield placed behind the highest energy experiment at 438 J exhibited a greater amount of damage as compared with the 251 J experiment, as shown in Fig. 19a and b. The plot in Fig. 19c clearly shows a greater number of fragments in the 438 J experiment. It should be noted that at comparable energy levels the damage accumulation on the glass shields decreased as the target thickness increased. For instance, the damage on the glass shield placed behind the 75 μm thick sample subjected to 167 J had much more damage than that placed behind the 250 μm sample subjected to 251 J. SEM analysis of the glass shields placed behind the 250 μm thick samples revealed much more melting/solidification of vanadium at the higher energy level of 438 J (Fig. 20).

3.4. Monocrystalline targets

The fracture morphology in the monocrystalline samples was quite different from the polycrystalline ones. Three marked differences were observed.

a. Fracture was characterized by both brittle and ductile morphologies. Fig. 21b shows evidence of cleavage on the back surface of the $\langle 1\,0\,0\rangle$ vanadium subjected to 36 J. This brittle fracture along [0 1 0] and [0 0 1] is in contrast to ductile fracture in the spall, seen in
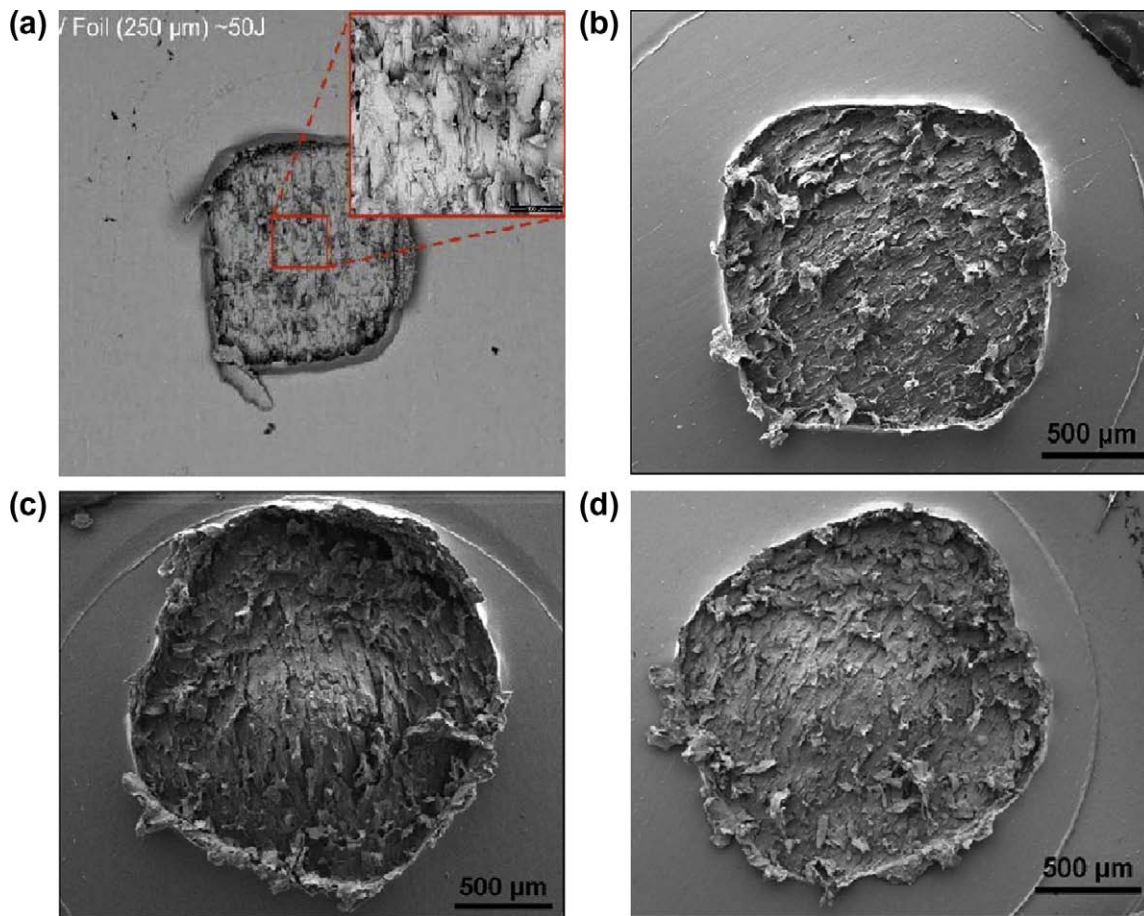
Fig. 16. Spalling of 250 μm samples; (a) 50 J, 3 ns; (b) 251 J, 3 ns; (c) 438 J, 3 ns; (d) 442 J, 3 ns.

Fig. 21c and d. Thus, the two modes occurred simultaneously. The ⟨1 1 0⟩ crystal also exhibited a mixture of ductile and brittle fracture, although the latter was more prevalent. The arrows in Fig. 22 mark the cleavage cracks. The ductile portion of fracture differs from that in the polycrystalline samples. This can be seen by comparing Fig. 11b with Figs. 21c and 22b. The dimples in the monocrystal were shallower, of lesser extent and less pronounced. An interesting phenomenon was also observed at high energies. The fracture surface in Fig. 22d shows a pattern that is unique and could be due to a molten or semi-molten state of the specimen.

b. The laser amplitude required to produce spalling (spall strength) was higher in the monocrystalline than in the polycrystalline samples. Whereas 50 J produced complete spallation in the polycrystalline sample (Fig. 16a), 86 J produced only partial separation (incipient spallation) in the monocrystal. This can be seen in Fig. 21a.

c. The number of fragments impacting on the glass plate was considerably lower for monocrystals than polycrystals. This is evident from Fig. 23 and is consistent for both orientations. If one compares these curves, at ~400 J energy, with the equivalent one in

Fig. 19 for a polycrystal having the same 250 μm thickness one can see that the number of fragments was considerably lower. Correspondingly, the central impact area was much larger for the monocrystal and
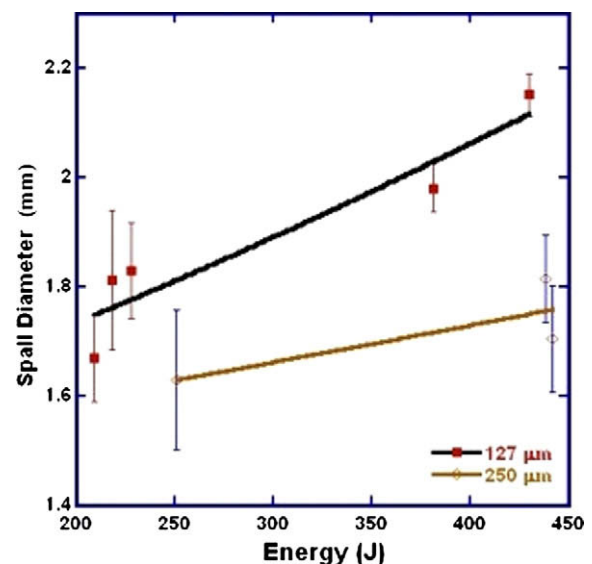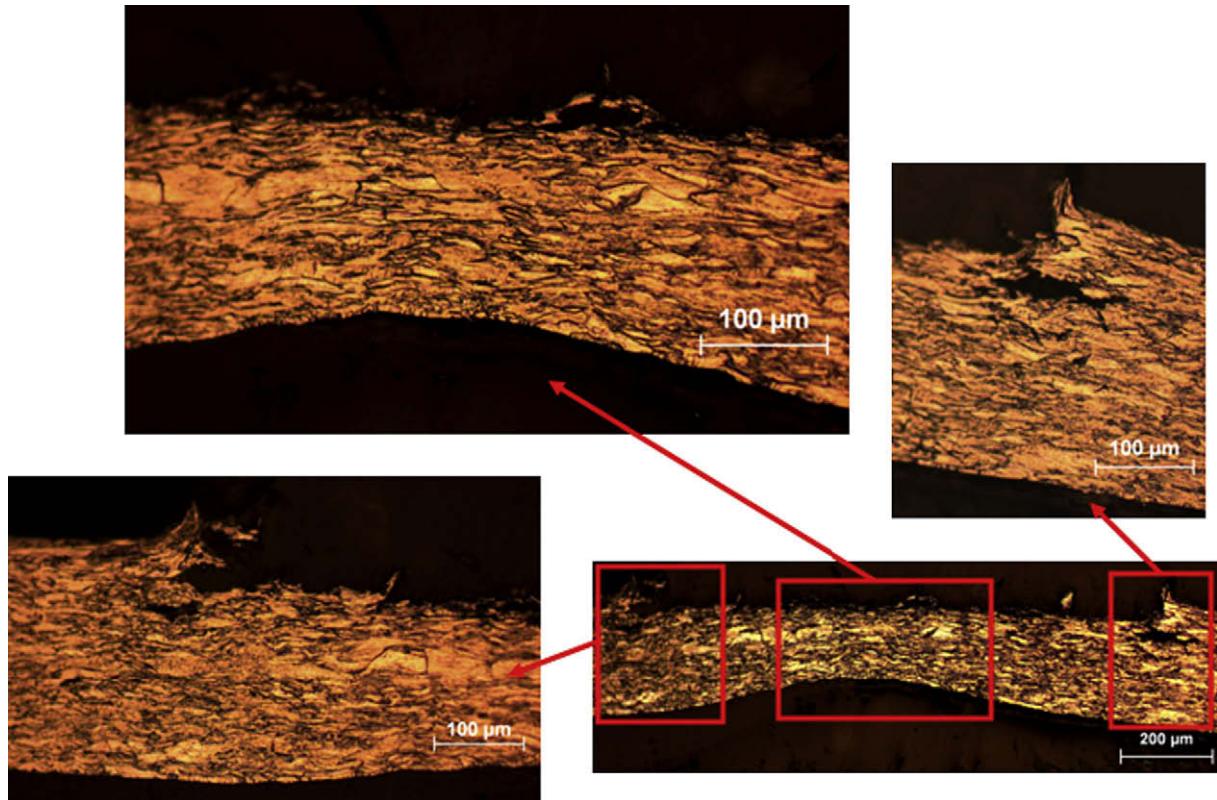

Fig. 17. Spall diameter vs. laser energy.

Fig. 18. Cross-section of 250 μm, 251 J, 3 ns showing the formation of incipient spall plane due to direct laser irradiation, flaking and ductile failure on spall plane, void formation and failure along grain boundaries.
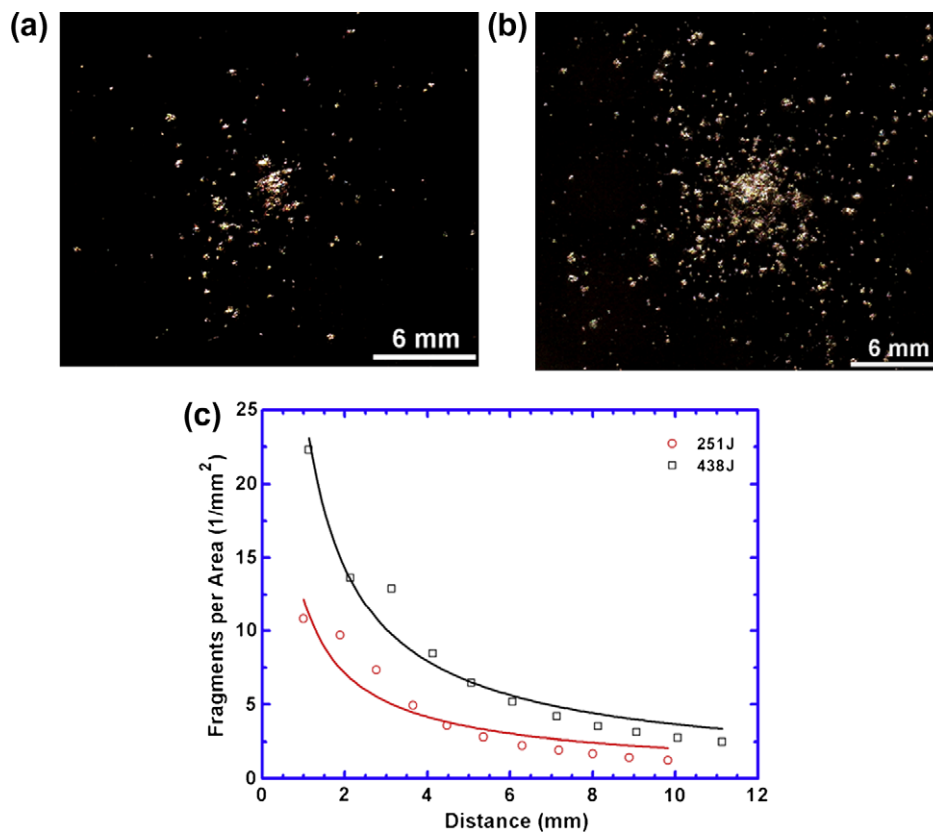

Fig. 19. Damage induced by 250 μm thick vanadium targets: (a) 251 J, 3 ns; (b) 438 J, 3 ns.
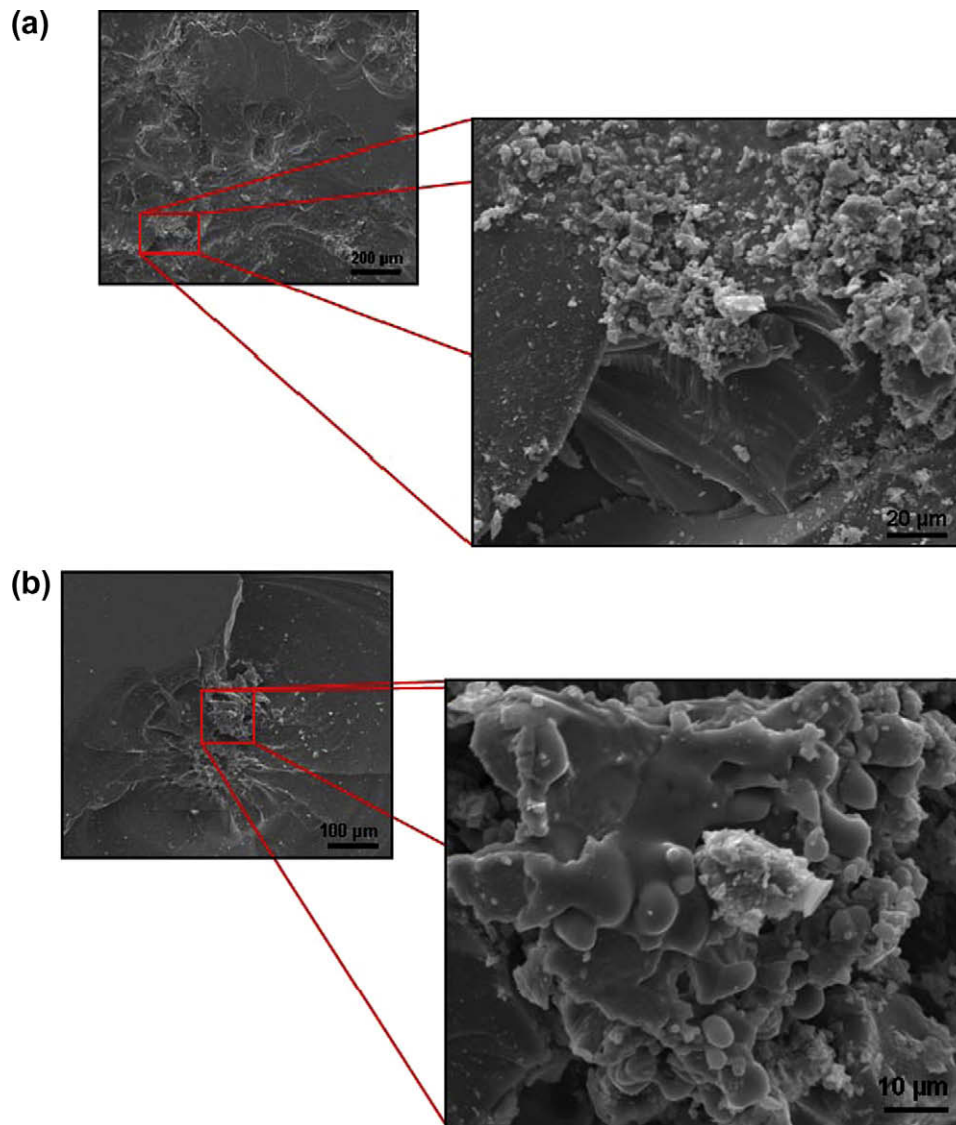
Fig. 20. Glass shield placed behind 250 μm thick target, 438 J, 3 ns: (a) debris and melting of vanadium around central crater; (b) melting on the surface of a vanadium fragment forming a subcrater away from the central crater.

this is evidence that the spall did not fragment as effectively in the latter. Figs. 19b and 23b show the same striking difference.

As discussed in the introduction, these differences are due to the fact that the polycrystal specimens fragment along grain boundaries, which are absent from monocrystals. This is also the reason why the monocrystal had a higher spall strength. Thus, microstructural aspects play a role in fragmentation.

3.5. Shadowgraph results

Gated shadowgraphy of the in-flight fragments was carried out for some monocrystals. We do not claim to have captured all the fragments but in the high energy shots the shadowgraphs show a well-formed plume. Fig. 24 shows images, while Fig. 25 shows the corresponding velocity distributions. A comparison of Fig. 24a and b suggests larger fragments for the $\langle 1\,0\,0 \rangle$ crystal, in agreement with a greater propensity for cleavage for this orientation. This indicates that cleavage leads to larger fragments, as suggested by the break-up of the sample in Fig. 21b. These results are also consistent with the markings on the glass target shown in Fig. 23b and c, indicating that the $\langle 1\,0\,0 \rangle$ crystal produced fewer fragments. One conclusion that can be reached from a comparison of the shadowgraph results with fragment impacts on the glass shields is that a sizable fraction of the fragments failed to produce visible craters on the glass surfaces. Approximately 200 fragments were counted for the $\langle 1\,1\,0 \rangle$ crystal, whereas the number seen in Fig. 23c is considerably lower. At the lower energies, as expected, the number of fragments and their velocities were lower (Fig. 25a and b).
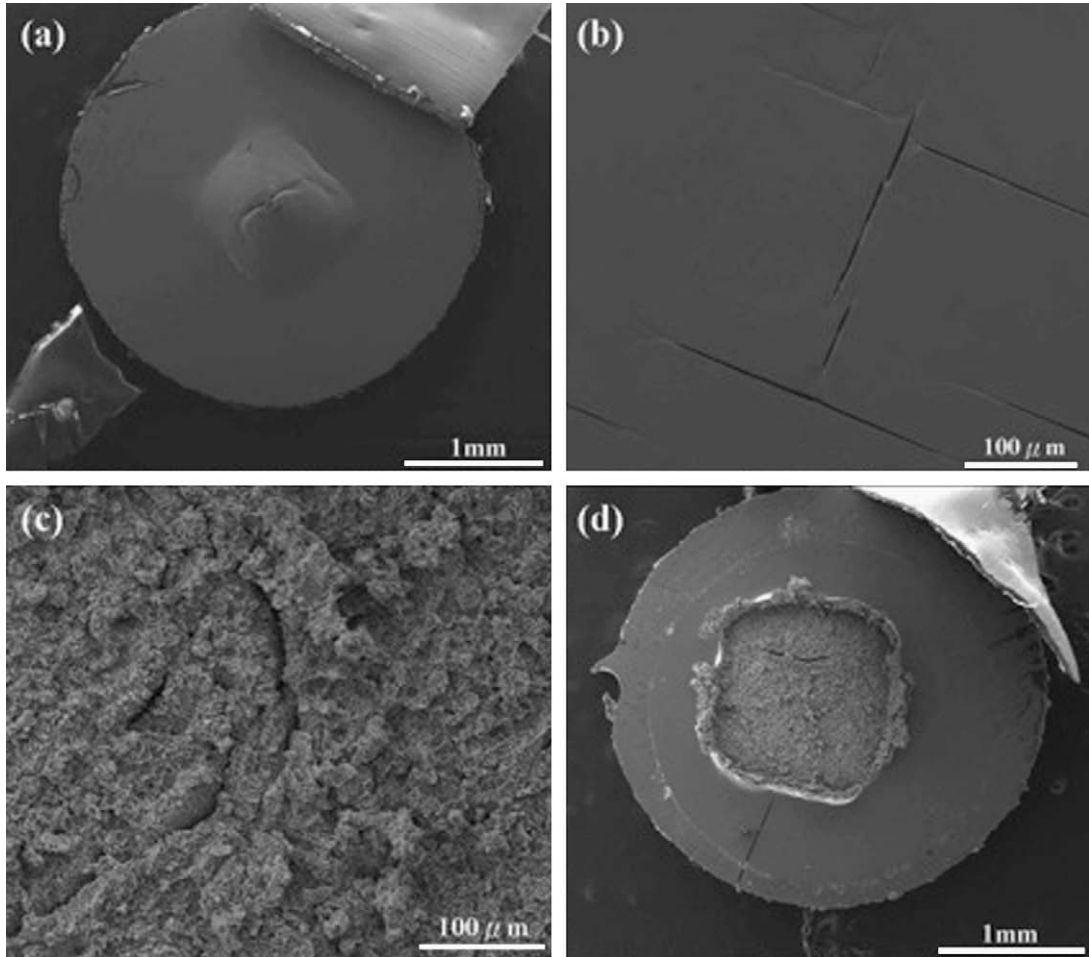
Fig. 21. Spalling of $\langle 1\,0\,0 \rangle$ monocrystals; (a) 86 J energy; (b) close-up of back surface of specimen subjected to 36 J energy showing cracks; (c) ductile fracture in sample subjected to 198 J; (d) spall surface of sample subjected to 198 J.

3.6. Fragment size modeling

The fragmentation of materials under high rate expansion has been treated extensively by Grady and co-workers [50–54]. The theoretical prediction of fragment size S when solid spall is dominated by flow stress is given by the Grady–Kipp (G–K) theory for ductile materials. This theory is based on energetic considerations, where the kinetic energy of an expanding body T and the elastic energy U are equated with the ductile fracture energy $W = Y\varepsilon_c$:

$$T + U \geqslant W \tag{12}$$

This leads to:

$$S = \left(\frac{8Y\varepsilon_c}{\rho \dot{\varepsilon}^2} \right)^{1/2} \tag{13}$$

where Y is the dynamic yield stress, ρ is the density, ε_c is the critical strain to failure and $\dot{\varepsilon}$ is the imposed strain rate. The strain rate in the current experiments can be estimated from the expansion of the spalled region as shown in the schematic of Fig. 26a. We assumed that

the spalled portion of the target was ejected in the form of an ellipse, with major axis a, equal to 1.25 mm (the inner radius of the washer sandwiching the target) and minor axis b, whose critical length before failure is to be calculated. Based on tensile experiments carried out on vanadium by Yoshinaga et al. [55], it was determined that vanadium fractures at a critical strain of $\sim$20%. Thus, the total circumference length of the ejected material at fracture must be $\sim$3 mm. From the equation of the perimeter of an ellipse, $P \approx \pi\sqrt{[2(a^2 + b^2)]}$, one can determine the length b of the minor axis (i.e. the distance traveled by the vanadium surface before failure). The expansion velocity can be approximated as the free surface velocity U_{fs}, which is equal to twice the particle velocity at the back surface ($U_{\text{fs}} \approx 2U_p$). Knowing the pressure at a given distance from the front surface from Figs. 3 and 4, U_p can be obtained from the Rankine–Hugoniot (R–H) equations. Thus, strain rates can be obtained from $2U_{\text{fs}}/P$.

Several investigators have studied the dynamic properties of vanadium under explosive loading [56], gas gun
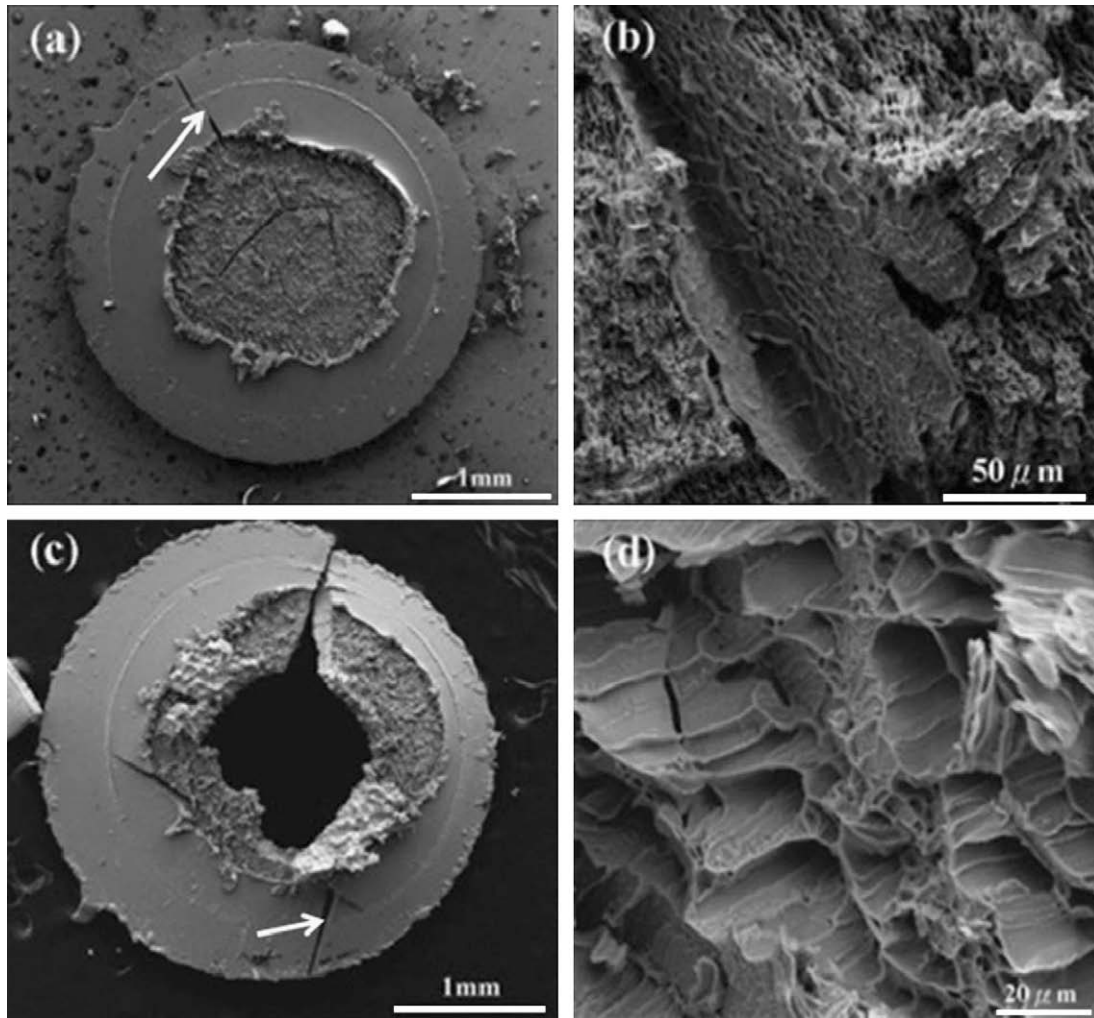
Fig. 22. Spalling of 250 um thick $\langle 1\,1\,0 \rangle$ monocrystal samples; (a) spall surface 392 J; (b) ductile separation; (spall surface 398 J); (d) fracture surface with deep dimples possibly due to partial melting.

loading [57] and the split Hopkinson pressure bar technique [58]. The dynamic yield stress was established to be ~480 MPa by Chabildas et al. [57], in very good agreement with work by Bat'kov et al. [56]. The yield strength of vanadium does not seem to be very sensitive to strain rate. Hence, we took the dynamic yield strength Y of vanadium to be 480 MPa in our analyses. With all parameters determined, the fragment size S_{G-K} is plotted as a function of strain rate in Fig. 26b.

We also directly determined the vanadium fragment sizes based on the number of fragments collected on the glass shields. Table 4 shows the different experiments carried out and the total number of fragments counted on the glass shields. The total number was estimated with the aid of the imaging software ImageJ. For simplicity, the assumption was made in all cases that the total spall area was $\pi d^2/4$, where $d = 2.5$ mm (the inner diameter of the washer), and the thickness of the fragments was equal to the spall thickness. Dividing the spalled area by the total number of fragments on the glass shield for all experimen-

tal cases, we were able to obtain the area of each individual fragment. Assuming the fragments were geometrically square and taking the square root of this area, we obtained the fragment size S_{exp}. The experimentally determined fragment sizes are also plotted as a function of strain rate in Fig. 26b.

It is clearly evident that the experimentally determined fragment sizes were smaller than those obtained using the G–K model by a factor of 2–3. One can get a better fit by increasing Y, but this is an uncertainty. More recent theories by Glenn and Chudnovsky [59] and Molinari and co-workers [60,61] predict values that were a factor of six lower than the original G–K model and, therefore, it can be said that the current experimental results are in between these. Considering the uncertainties in experimental measurements and simplifying the assumptions in the G–K model, the agreement is considered satisfactory. Theory predicted and the experiments showed a decrease in fragment size with strain rate. The S_{exp} values were actually in better agreement with some fragment sizes measured
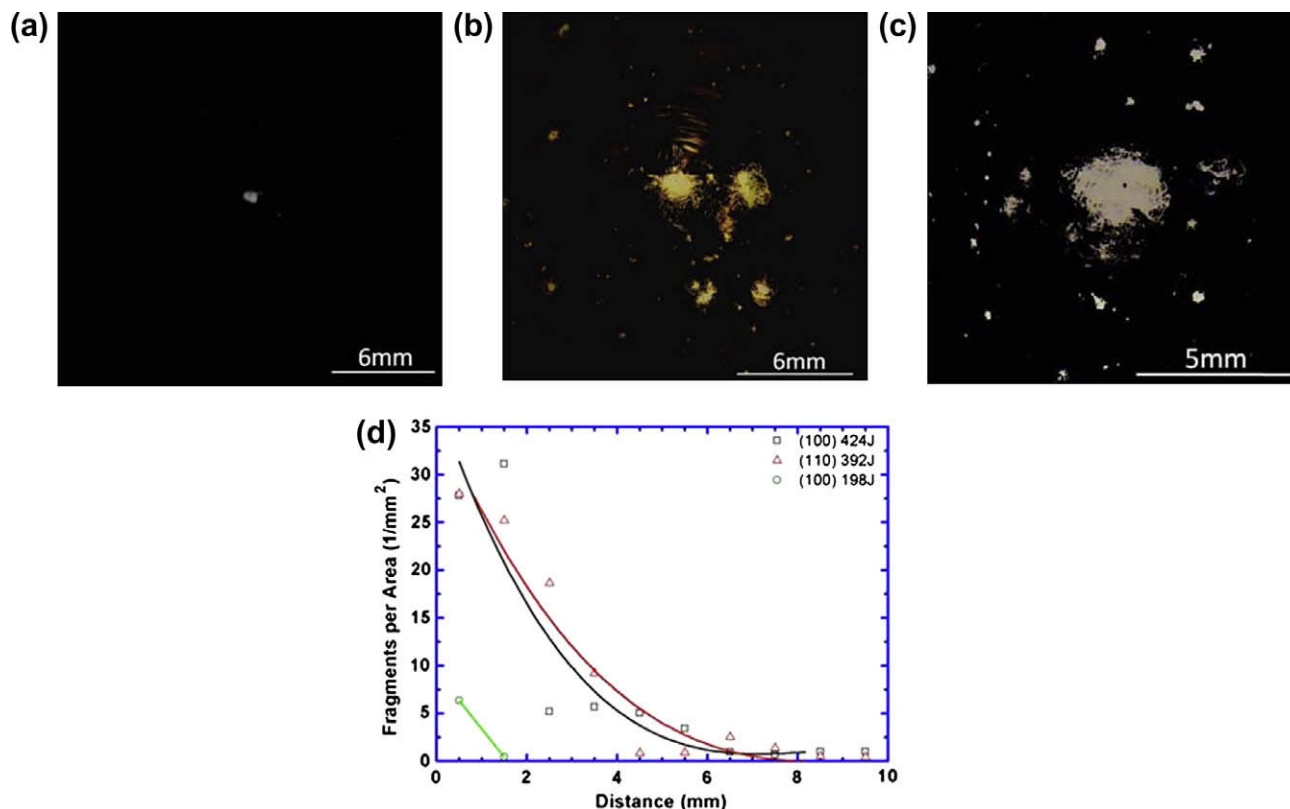
Fig. 23. Damage in monocrystalline 250 μm vanadium targets: (a–c) glass shields damaged by monocrystalline vanadium fragments: energies of 198 J ($\langle 1\,0\,0\rangle$), 424 J($\langle 1\,0\,0\rangle$), 392 J ($\langle 1\,1\,0\rangle$), respectively; (d) fragments per area as a function of distance from central damage.

from SEM micrographs of the glass shield surfaces. The sizes obtained from the G-K theory provided an overestimate. In particular, preliminary experiments (Maddox, unpublished results) indicate that the free surface velocity was one-quarter of that calculated herein. The fragments decelerated from the initial expansion velocity of the spall because deformation and fragmentation consume energy. This lower free surface velocity would shift the G–K curve to the left and bring the predicted results closer to the experimental ones.

3.7. Spall strength determination

Values for the spall strength (σ_{spall}) of vanadium are absent in the literature, and an attempt to measure this value was made here. Two methods of estimating the spall strength of the specimens were used.

3.7.1. Thickness of the spall layer

This method was explained by Gilath [38] and is shown in Fig. 5 and explained in Section 3.1. It is possible to determine σ_{spall} based on the experiments carried out on the 250 μm targets, since a spall surface clearly developed in those experiments. We use the spall thickness measured from the optical micrographs (as in Figs. 11 and 16) to aid in our calculations. From the micrographs we estimated a spall thickness of ~30 μm for the 251 J experiment

(and ~50 μm for the 438 J experiment, figure not shown). The basic physics of waves was used to determine the tensile stress that developed at the spall plane. This is explained in Section 3.1 (Eq. (4)). Using the HYADES computations we could determine the magnitude of the tensile stresses at these depths. The estimated spall strengths using the pulse decay calculations were 9 GPa for the 250 J experiment and 18 GPa for the 438 J experiment (Fig. 4a and 4b). Using the HYADES computations (Fig. 4c and 4d), the tensile stress was approximately 10 GPa. Clearly, a strain rate effect on the spall strength existed, as previously observed by others (e.g. works by Gilath [38] and Wang et al. [62] on laser-shocked aluminum).

3.7.2. VISAR pull-back signal

This technique is known to provide reliable estimates of the spall strength. It was calculated from pull-back signals in the experiments carried out on the monocrystals of 250 μm thickness. The procedure was delineated by Grady and Kipp [63]. The following expression was used for the spall strength (Eq. (8.7) from Grady and Kipp [63]):

$$\sigma_{\text{T}} = \frac{1}{2}(Z_{\text{s}} - Z_{\text{w}})u_{\text{max}} - \frac{1}{2}(Z_{\text{s}} + Z_{\text{w}})u_{\text{min}} \qquad (14)$$

where u_{max} and u_{min} are the velocities marked A and B in Fig. 27 and the impedances of the window and specimen
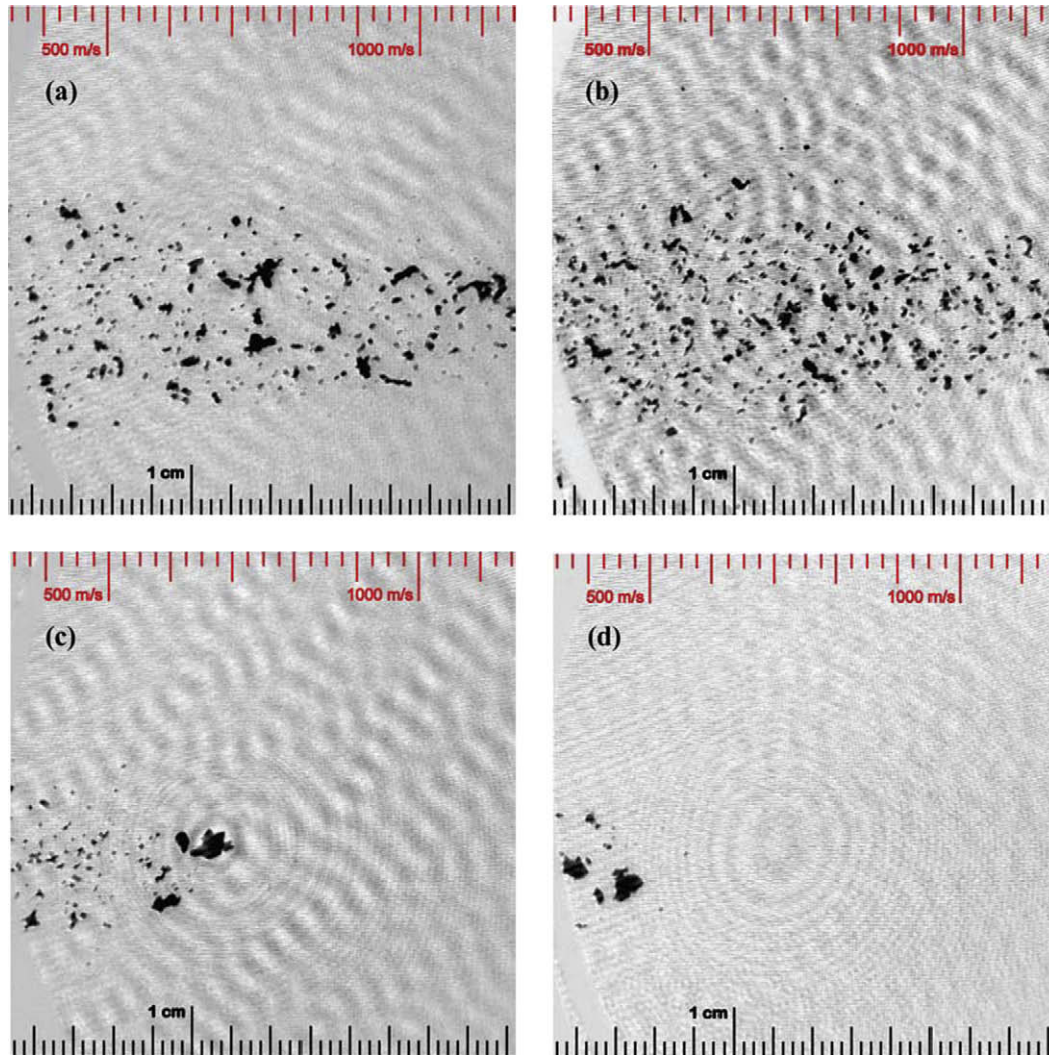
Fig. 24. Gated shadowgraphy of in-flight particles ejected from: (a) $\langle 1\,0\,0 \rangle$ at 415 J, (b) $\langle 1\,1\,0 \rangle$ at 423 J, (c) $\langle 1\,1\,0 \rangle$ at 206 J, and (d) $\langle 1\,1\,0 \rangle$ at 106 J.

are Z_w and Z_s, respectively. Since VISAR was applied directly to the surface of the specimen $Z_w = 0$. Thus:

$$\sigma_T = \frac{1}{2} \rho_0 C_0 (u_{max} - u_{min}) \tag{15}$$

where $\rho_0 = 6.11 \times 10^3 \text{ kg m}^{-3}$ and $C_0 = 4560 \text{ m s}^{-1}$ for vanadium. The calculated spall strengths for the 423, 206 and 106 J experiments were 8.8, 4.8 and 5.6 GPa, respectively. These values are consistent with the calculations using the spall plane thickness. The HYADES calculations predicted a spall strength of 10 GPa; the less accurate calculations from the estimate predicted values between 9 and 18 GPa. The VISAR free surface velocity traces were also converted into pressure vs. time plots using the R–H relations and shock equation of state for vanadium. The results are shown in Fig. 27b and c. The pressures at the back surface were compared with predictions from HYADES simulations (points in plots) and the results compared favorably.

Grady [39] developed explicit expressions for the spall strength of condensed media. He derived an equation for the theoretical cleavage strength, which gives an upper bound value. The theoretical cleavage strength, which is the highest possible value for the spall strength, is derived from an analytical representation of the cold compression–tension curve based on a Morse potential and is of the form [39]:

$$\sigma_{th} = \sqrt{\frac{U_{coh} B_o}{8 V_o}} \tag{16}$$

where U_{coh} is the specific cohesive energy (10.04 MJ kg^{-1} for vanadium, calculated from [65,66]), B_o is the bulk modulus (160 GPa for vanadium) and V_o is the specific volume at zero pressure. Eq. (16) gives a theoretical cleavage strength of $\sim$35 GPa. Fig. 28 presents the theoretical cleavage strengths plotted against the bulk modulus B_o. There is an approximate linear relation. Based on a simpler Orowan calculation one obtains:
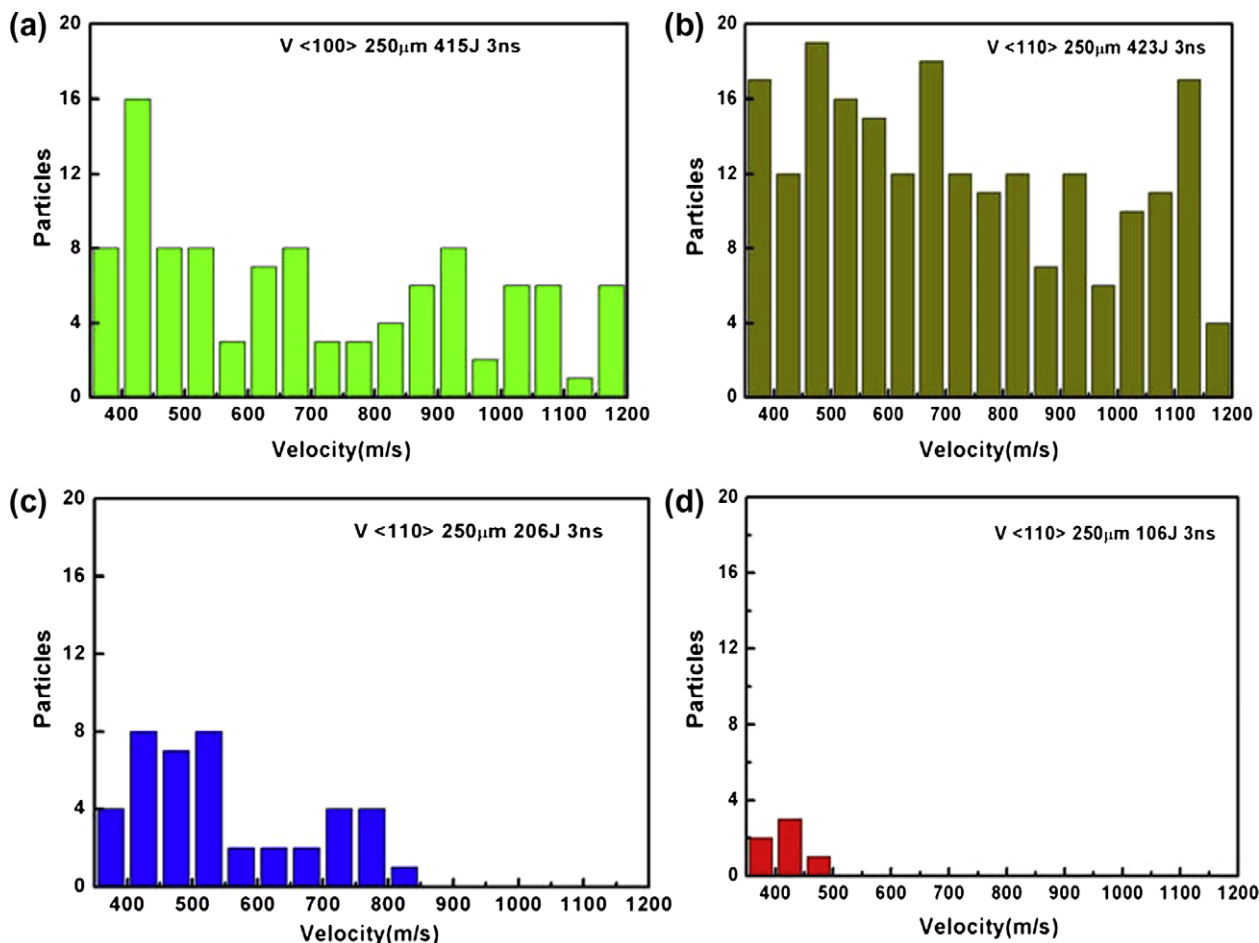
$$\sigma_{th} = \frac{B_o}{\pi} \tag{17}$$

Fig. 25. Fragment velocity distribution from gated shadowgraphs in Fig. 24: (a) $\langle 1\,0\,0 \rangle$ at 415 J, (b) $\langle 1\,1\,0 \rangle$ at 423 J, (c) $\langle 1\,1\,0 \rangle$ at 206 J, and (d) $\langle 1\,1\,0 \rangle$ at 106 J.

This provides a value of ∼50 GPa for V. So, both equations provide theoretical maximum spall strengths that are approximately proportional to the bulk modulus.

In line with this, spall results (primarily obtained in gas gun experiments) are presented in Fig. 28 for a number of metals and compared with the G–K formulation, originally proposed by Grady [39]. Using an energy balance analysis, Grady [39] also provided expressions for both the ductile and brittle spall strengths of condensed media, which provided values that were more consistent with the experimental results using gas guns. Table 5 presents the theoretical spall strengths of various common fcc and bcc metals. From the SEM analysis it is safe to conclude that vanadium spalls by ductile behavior (see Fig. 11c). In other words, the spall process involves the nucleation, growth and coalescence of voids) and occurs strictly through plastic flow. Hence, we adopt the Grady expression for ductile spall [39]:

$$\sigma_T = (2\rho c_o^2 Y \varepsilon_c)^{1/2} \qquad (18)$$

where ρ is the density, c_o is the velocity of sound at zero pressure, Y is the dynamic yield strength (480 MPa) and ε_c is the critical strain (0.2). This expression gives a spall strength of 5.5 GPa for vanadium. Fig. 28 shows the theoretical ductile spall strength of vanadium and various other fcc and bcc metals and how they compare with the experimental results tabulated by Meyers et al. [44] from different sources, also given in Table 5.

Most of the theoretical ductile spall strengths of the various materials reported by Grady [39] seem to be in the same range as the experimental values (Table 3 in Grady [39]). It should be mentioned that these experiments were conducted using gas guns. The experimental values obtained herein for vanadium using lasers were higher than the calculated Grady [39] ductile spall strengths (Eq. (18)), by a factor of up to 2. Our results are consistent with those of Gilath [38], who measured the spall strength of aluminum and 6061-T6 aluminum (2.5–5 GPa) at a strain rate of $1–4 \times 10^7 \, s^{-1}$ produced by laser shock under conditions similar to those in the present investigation. In contrast, gas gun measurements reported by Grady [39] at strain rates of $10^4–10^6 \, s^{-1}$ showed a spall strength of 1–2 GPa (Fig. 9 in Grady [39]).

For copper there are laser results by Moshe et al. [67] reporting a spall strength of 9.5 GPa and results by Schneider [68] reporting a value of 5 GPa. Both values
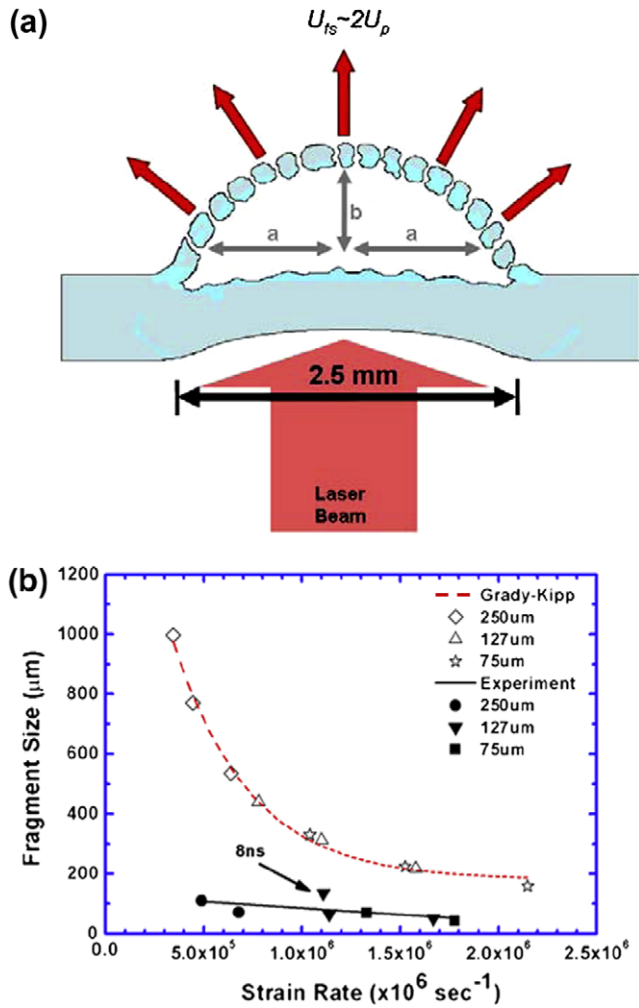
(a)

(b)

Fig. 26. Illustration of the expansion of the spalled surface used in the Grady–Kipp model; (b) fragment size vs. strain rate.

Table 4
Total number of fragments counted on glass shields for various experiments.

Sample thickness (μm)	Laser energy level (J)	Total no. of fragments
75	167	1031
75	290	2603
127	218 (8 ns)	270
127	228	1150
127	430	1914
250	251	371
250	438	956

b. Spalling is a nucleation–growth–coalescence process. The treatments developed by Curran et al. [69,70] and applied by Deckel et al. [71] deal with this by incorporating a time and stress dependence of the concentration of nucleation sites and void growth velocity.

4. Conclusions

The following are the principal conclusions.

1. Evidence of molten and resolidified fragments was observed, in agreement with a solid–liquid transition induced by shock compression, which was calculated to be 150 GPa.
2. The damage and fragment distribution were significantly affected by laser energy. The highest intensity experiments resulted in a high density of very small droplets distributed on the glass plate, while the lowest intensity experiments resulted in a few damaged spots on the glass plates.
3. Thicker foils (250 μm) showed incipient spall planes and bulk deformation by shock loading, samples of intermediate thickness (127 μm) showed tearing away around the laser spot, while the thinnest foils (75 μm) showed almost complete blow-off due to the laser beam interaction. At the same energy level damage accumulation on the glass shields decreased as the target thickness increased.
4. In the monocrystalline samples there were clear differences: a higher spall strength and the appearance of cleavage cracks associated with brittle fracture. This is in accordance with enhancement of the ductile–brittle transition increasing the grain size.
5. Spalling and fragmentation were found to proceed by ductile void nucleation, growth and coalescence. The grain boundaries were favored paths for decohesion.
6. The fragmentation was quantitatively estimated as a function of laser pulse energy and duration and compared with the G–K analysis. The measured spall strengths were higher, by a factor of 2–3, than the expected results and calculations using G–K analysis. The discrepancy can be attributed to the strain rate sensitivity of the yield stress, which is considered satisfactory in view of the experimental uncertainties and theoretical assumptions. Other factors, such as the spall thickness, could also play a role.
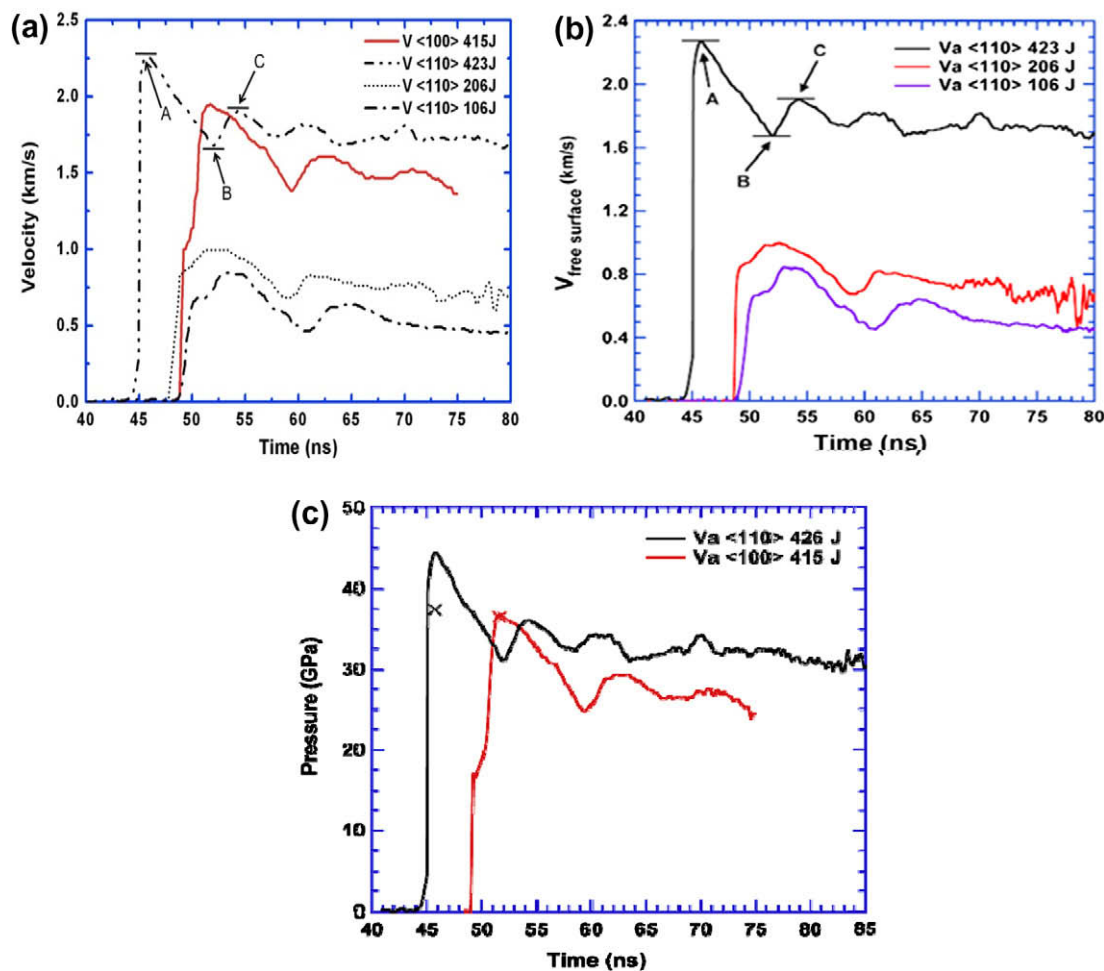
are considerably higher than those reported for gas gun experiments and using the G–K equation. In Fig. 28 two lines are drawn, corresponding to gas gun and laser experiments.

So, there is a clear time dependence of spall strength on strain rate (or time), which could have two possible reasons.

a. Eq. (18) has a term Y, the yield stress, which exhibits a strain rate dependence that can be expressed, to a first approximation, by the power function:

$$Y = Y_0 \left(\frac{\dot{\varepsilon}}{\dot{\varepsilon}_0} \right)^m \tag{19}$$

where $\dot{\varepsilon}$ is the strain rate and m is the strain rate sensitivity. Thus, the spall strength would have a strain rate dependence of $m/2$, if the other two parameters in Eq. (19) are normalizing factors. If one considers that the strain rates imparted by a gas gun and laser compression are of the order of 10^4–10^6 s^{-1} and by laser compression of the order of 10^7 s^{-1} one would arrive at a reasonable agreement.

Fig. 27. (a) Free surface velocity and (b) pressure as a function of time for Va ⟨1 1 0⟩ single-crystal samples at 423 J, 206 J, and 106 J. The values at A, B, and C correspond to the peak velocity, pull-back velocity, and spall peaks. (c) Pressure as a function of distance for ⟨1 1 0⟩ and ⟨1 0 0⟩ single-crystal samples at laser energies 426 J and 415 J, respectively, calculated using the free surface velocity measured from VISAR and V RH shock data. Single points are peak pressure values calculated using the HYADES code.

Table 5
Theoretical and experimental spall strengths of various metals.

Element	Bulk modulus (GPa)	Theoretical cleavage stress (GPa)	Ductile spall strength (GPa)	
			Theoretical	Experimental
Al	72	17.1	0.57–0.81	0.5–1.1
Cu	137	28.5	1	1–2.5
V	160	35	5.5	9–18
Fe	168	35	–	1.6–4.5
Ta	200	42.4	6.5	4.4–6.8

7. Shadowgraph pictures reveal the fragment distribution for the monocrystalline experiments, which can be successfully correlated with the fragments measured on the glass and polycarbonate targets and allow determination of the velocity distributions.

8. VISAR velocimetry measurements were carried out on the monocrystalline specimens. The pressures at the back surface were compared with HYADES predictions and good agreement was obtained.

9. Both the spall thickness and pull-back signals from VISAR velocimetry were used to estimate the spall strength. The spall thickness was used in combination with the calculated decay of the shock pulse. It was found to be in the range of 9–18 GPa. The spall strengths obtained from VISAR pull-back signals were lower, in the range 5–9 GPa. These results are higher than the experimental results obtained using gas guns and consistent with laser compression results. The differences can be attributed to two causes.

a. The strain rate sensitivity of the flow stress, incorporated in the Grady [39] prediction.

b. Spalling being the result of the nucleation, growth and coalescence of voids/cracks, which are time-dependent phenomena. (A complete analytical prediction has to involve this phenomenology, first proposed by Curran et al. [69,70] and further developed by Deckel et al. [71], and also discussed by Grady [64].)
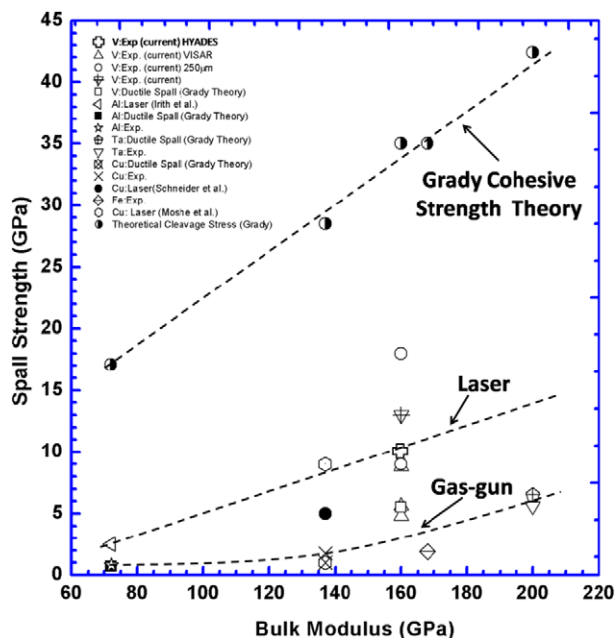
Fig. 28. Spall strength vs. bulk modulus for various fcc and bcc metals; comparison of theoretical cleavage strength (Grady [39], upper curve) and experiments. Note separate curves for gas gun and laser experiments suggesting a strong strain-rate or time dependence.

Acknowledgements

References

[1] Kurtz RJ, Hamilton ML, Li H. J Nucl Mater 1998;258–263:1375.
[2] Zinkle SJ, Matsui H, Smith DL, Rawcliffe AF, ven Osch E, Abe K, et al. J Nucl Mater 1998;258–263:205.
[3] Kurtz RJ, Abe K, Chernov VM, Kazatov VA, Lucas GE, Matsui H, et al. J Nucl Mater 2000;283–287:70.
[4] Meyers MA, Aimone CT. Prog Mater Sci 1983;28:1.
[5] Davidson L, Graham RA. Phys Rep 1979;55:255.
[6] Curran DR, Seaman L. Phys Rep 1987;147:253.
[7] McQueen RG, Marsh SP. J Appl Phys 1962;33:654.
[8] Vidal F, Johnston TW, Laville S, Barthélemy O, Chaker M, Le Drogoff B, et al. Phys Rev Lett 2001;86:2573.
[9] Kanel GI, Fortov VE. Adv Mech 1987;10:3.
[10] Rosenberg L, Luttwak G, Yeshurun Y, Partom Y. J Appl Phys 1983;54:2147.
[11] Chen D, He H, Jing F. J Appl Phys 2007;102:1.
[12] Andriot P, Chapron P, Lambert V, Olive F. Shock waves in condensed matter. Amsterdam: Elsevier; 1983. p. 277.
[13] Rybakov AP, Rybakov IA. Eur J Mech B Fluids 1995;14:197.
[14] Zhiembetov AK, Mikhaylov AL, Smirnov GS. AIP Conf Proc 2002;620:547.
[15] Holtkamp DB, Clark DA, Garcia IA. AIP Conf Proc 2004;705:473.
[16] Holtkamp DB, Clark DA, Garcia A. AIP Conf Proc 2004;705:477.
[17] Fox JA, Barr DN. Appl Phys Lett 1973;22:594.
[18] Cottet F, Boustie M. J Appl Phys 1989;66:4067.
[19] Eliezer S, Gilath I, Bar-Noy T. J Appl Phys 1990;67:715.
[20] Eliezer S, Gazit Y, Gilath I. J Appl Phys 1990;68:56.
[21] Boustie M, Cottet F. J Appl Phys 1991;69:7533.
[22] (a) Lacomme M, Cazalis B, David J, Niérat G, Salères A, Sibille G. J Phys (France) IV Colloq 1994;8(Supp):77;
(b) Lacomme M, Cazalis B, David J, Niérat G, Salères A, Sibille G. J Phys (France) III 1994;4:77.
[23] de Rességuier T, Cottet F. J Appl Phys 1995;77:3756.
[24] Remington BA, Bazan G, Belak J, Bringa E, Caturla M, Colvin JD, et al. Met Mater Trans 2004;35A:2587.
[25] Meyers MA, Gregori F, Kad BK, Schneider MS, Kalantar DH, Remington BA, et al. Acta Mater 2003;51:1211.
[26] Schneider MS, Kad B, Kalantar DH, Remington BA, Kenik E, Lubarda V, et al. Int J Impact Eng 2005;32:473.
[27] Hawreliak J, Colvin JD, Eggert JH, Kalantar DH, Lorenzana HE, Stölken JS, et al. Phys Rev B 2006;74:184107.
[28] Wang Y, He H, Boustie M, Sekine T. J Appl Phys 2007;101:103528.
[29] Meyers MA, Schneider MS, Jarmakani H, Kad B, Remington BA, Kalantar DH, et al. Met Trans 2007;39A:304.
[30] Cao BY, Meyers MA, Lassila DH, Schneider MS, Kad BK, Huang CX, et al. MSE A 2005;409:270.
[31] de Rességuier T, Signor L, Dragon A, Boustie M, Roy G, Llorca F. J Appl Phys 2007;101:013506.
[32] Lubarda VA, Meyers MA, Schneider M, Remington B, Kalantar D. Acta Mater 2004;52:1397.
[33] Christy S, Pak HR, Meyers MA. In: Murr LE, Staudhammer KP, Meyers MA, editors. Metallurgical applications of shock-wave and high-strain rate phenomena. New York: Marcel Dekker; 1991. p. 775.
[34] Kanel GI, Rasorenov SV, Fortov VE. In: Shock-wave and high-strain rate phenomena in materials. New York: Marcel Dekker; 1991. p. 775.
[35] Meyers MA. In: Meyers MA, Armstrong RW, Kirchner HOK, editors. Mechanics and materials: fundamentals and linkages. New York: Wiley; 1999. p. 489–594.
[36] Koller DD, Hixson RS, Gray GT, Rigg PA, Addesio LB, Cerreta EK, et al. J Appl Phys 2005;98:103518.
[37] Gray GT, Bourne NK, Henrie BL. J Appl Phys 2007;101:093507.
[38] Gilath I. In: Davison L, Grady DE, Shahinpoor M, editors. High-pressure shock compression of solids. New York: Springer; 1996. p. 90–120.
[39] Grady DE. J Mech Phys Solid 1988;36:353.
[40] Barker LM, Hollenbach RE. J Appl Phys 1972;43:4669.
[41] Celliers PM, Collins GW, Da Silva LB, Gold DM, Cauble R. Appl Phys Lett 1998;73:1320.
[42] Barker LM, Schuler KW. J Appl Phys 1974;45:3692.
[43] Samsonov GV, editor. Handbook of the physicochemical properties of the elements. New York: IFI Plenum; 1968. p. 383.
[44] Meyers MA. Dynamic behavior of materials. New York: John Wiley; 1994.
[45] Sorkin V, Polturak E, Adler J. Phys Rev B 2003;68:174102.
[46] Jephcoat AP, Besedin S. In: Manghnani M, Yagi T, editors. US–Japan conference on mineral physics. Washington (DC): AGU; 1997.
[47] Errandonea D, Schwager B, Ditz R, Gessmann C, Boehler R, Ross M. Phys Rev B 2001;63:132104.
[48] McQueen RG, Marsh SP, Taylor JW, Fritz JN, Carter WJ. In: Kinslow R, editor. High velocity impact phenomena. New York: Academic Press; 1970.
[49] Dai C, Jin X, Zhou X, Liu J, Hu J. J Phys D Appl Phys 2001;34:3064.
[50] Grady DE, Kipp ME. Int J Rock Mech Min Sci Geomech 1979;17:147.

[51] Grady DE, Kipp ME. Int J Rock Mech Min Sci Geomech 1979;16:293.

[52] Grady DE, Kipp ME. Mech Mater 1985;4:311.

[53] Kipp ME, Grady DE, Swegle JW. Int J Impact Eng 1993;14:427.

[54] Grady DE, Kipp ME. Int J Impact Eng 1997;20:293.

[55] Yoshinaga H, Toma K, Abe K, Morozumi S. Philos Mag 1971;23:1387.

[56] Bat'kov YV, Glushak AB, Glushak BL, Novikov SA, Fishman ND. Combust Explos Shock Waves 1995;31:605.

[57] Chabildas LC, Hill CR. In: Murr LE, Staudhammer KP, Meyers MA, editors. Metallurgical applications of shock wave and high strain-rate phenomena. New York: Marcel Dekker; 1986. p. 429–48.

[58] Lennon AM, Ramesh KT. Int J Plast 1998;14:1279.

[59] Glenn LA, Chudnovsky A. J Appl Phys 1986;59:1379–80.

[60] Mariot C, Michaut V, Molinari JF. In DYMAT 2009, proceedings of the 9th international conference on the mechanical and physical behavior of materials under dynamic loading, 2009. p. 1523.

[61] Zhou F, Molinari JF, Ramesh KT. Comput Mater Sci 2006;37: 74–85.

[62] Wang Y, He H, Wang L, Jing BoustieFM, Sekine T. J Appl Phys 2006;100:033511.

[63] Grady DE, Kipp ML. In: Asay JR, Shahinpoor M, editors. High-pressure shock compression of solids. New York: Springer; 1993. p. 265–322.

[64] Grady DE. In: Gronig H, Horie Y, Takayama K, editors. Shock wave science and technology reference library, vol. 3. New York: Springer; 2009. p. 169–276.

[65] Kittel C. Introduction to solid-state physics. 5th ed. New York: Wiley; 1983.

[66] Rose JH, Smith JR, Guinea F, Ferrante J. Phys Rev B 1984;29:2963.

[67] Moshe E, Eliezer S, Deckel E, Ludminsky A, Henis Z, Goldberg IB, et al. J Appl Phys 1998;83:4004.

[68] Schneider MS. Doctoral dissertation, University of California San Diego.

[69] Curran DR, Seaman L, Shockey DA. Phys Today 1977;30:46.

[70] Curran DR, Seaman L, Shockey DA. Phys Lett 1987;147:253.

[71] Dekel E, Eliezer S, Henis Z, Moshe E, Ludminsky A, Goldberg IB. J Appl Phys 1998;84:4851.